https://doi.org/10.5194/egusphere-2026-4904
Preprint. Discussion started: 3 November 2026
© Author(s) 2026. CC BY 4.0 License.

"

High-resolution 3D turbulence measurements with different quadcopter uncrewed aerial systems: verification and validation for single- and multi-vehicle measurements

Johannes Kistner[1,3], Thomas Messmer[2], Joachim Peinke[3,4], and Norman Wildmann[1]

[1]Deutsches Zentrum für Luft- und Raumfahrt, Institut für Physik der Atmosphäre, Oberpfaffenhofen, Germany
[2]École Polytechnique Fédérale de Lausanne (EPFL), Lausanne 1015, Switzerland
[3]Carl von Ossietzky Universität Oldenburg, School of Mathematics and Science, Institute of Physics
[4]ForWind - Center for Wind Energy Research, Küpkersweg 70, 26129 Oldenburg, Germany

Correspondence: Johannes Kistner (johannes.kistner@dlr.de)

Abstract. The SWUF-3D drone fleet is used to obtain in situ measurements of three-dimensional turbulence in the atmospheric boundary layer (ABL). This requires high measurement accuracy and a quantification of measurement uncertainties. Hardware modifications can extend flight duration but may also alter flight behavior. Because wind estimates are derived from forces inferred from avionics data, the open question is how far turbulence measurements become affected by such modifications. We therefore quantify hardware-dependent resolvable frequency ranges and uncertainties for single-point and multi-point turbulence statistics. Since we perform simultaneous, spatially distributed fleet measurements with the drones, we also assess the capabilities and limitations of such multi-location measurements. To determine the uncertainties, we perform verification under laboratory conditions and validation under real-world conditions against reference sensors using different hardware configurations. Using the main hardware configuration of the drones, we perform fleet measurements of the 3D wind vector with spatial separations in all directions to evaluate measurements for the analysis of velocity increments and coherence. The dataset comprises 42 wind tunnel time series of approximately 10 min and 155 field flight time series with an average duration of more than 10 min. We identify hardware-dependent maximum resolvable frequencies of approximately 2.5–5 Hz, with the main configuration capable of resolving frequencies up to 3.5 Hz. Variance estimates are comparable across configurations, with a root mean square error of $\leq 0.21\ \mathrm{m^2\,s^{-2}}$. Within the resolvable frequency ranges, the probability density functions (PDFs) of velocity increments agree well with those derived from reference sensors down to a minimum resolved spatial lag of 2 m. At very short lags and low wind speeds, extreme deviations from Gaussianity (i. e. intermittency) are not fully captured, which leads to an underestimation of the kurtosis of the velocity increment PDFs. Fleet measurements resolve spatial velocity increments and coherence for the 3D wind components in all three separation directions at distances of 50–100 m. All drone configurations resolve the frequency range over which coherence is observed. The SWUF-3D fleet can reliably measure turbulence statistics within hardware-dependent small-scale limits, which mainly affect the quantification of intermittency at small scales. The fleet measurements enable spatial two-point analyses of turbulence in all directions. The quantified effects and uncertainties provide a basis for future ABL turbulence studies, for example in complex terrain and wind turbine wakes.

https://doi.org/10.5194/egusphere-2026-4904
Preprint. Discussion started: 3 November 2026
© Author(s) 2026. CC BY 4.0 License.

1 Introduction

Reliable measurements of wind and turbulence are essential for understanding atmospheric boundary layer (ABL) processes and for improving applications such as wind energy assessment and meteorological observations (Stiperski et al., 2025; Kosović et al., 2026). However, conventional in situ measurement systems are often limited in their spatial flexibility and vertical reach. Uncrewed aerial systems (UASs) have been established as an alternative, enabling measurements in environments and at altitudes that are difficult to access with stationary measurement infrastructure.

UAS platforms used for ABL observations can generally be divided into fixed-wing systems (Wildmann et al., 2015; Rautenberg et al., 2019; Bramati et al., 2025) and rotary-wing systems. The latter offer practical advantages, notably the ability to hover in a stationary position. Within this category, measurements using multicopter UASs can be further divided into two main approaches. In the direct approach, the UAS primarily serves as a carrier platform for specialized anemometers (Molter and Cheng, 2020; Thielicke et al., 2021; Ghirardelli et al., 2025; Yang et al., 2025). In the indirect approach, the drone itself serves as an anemometer by deriving the wind vector from avionics data (Neumann and Bartholmai, 2015; Palomaki et al., 2017; Brosy et al., 2017; Shelekhov et al., 2022; Chen et al., 2026; Segales et al., 2026).

Using the indirect method with copter-UAS, analyses are conducted with the SWUF-3D fleet (Wetz et al., 2021) to perform high-resolution wind measurements in the mountain boundary layer (Pfister et al., 2024) and wind turbine wakes (Wildmann and Kistner, 2024, 2025) using up to 30 drones simultaneously. Wind measurements have already been calibrated for horizontal winds (Kistner et al., 2024) and vertical winds (Kistner et al., 2026), and the accuracy of wind speed measurements has been quantified. For future data analyses of spatially distributed fleet measurements of 3D turbulence in the ABL, measurement capabilities with the highest possible resolution and accuracy are required, as is an understanding of the uncertainties in these measurements. Additionally, the drone hardware is continuously being adapted to increase the flight duration of the drones and thus the measurement duration.

While in the direct method the error in the sensor signal is driven by sensor positioning or propeller induction, the propeller-induced flows need to be well described and measured. In the indirect method, the flight physics of the drone needs to be well described and measured to derive a wind estimate. Hardware modifications, such as propeller or battery upgrades, can change the flight physics, including thrust, lift, and drag, and thus directly affect the wind measurement. An assessment of the effects of hardware modifications is therefore important for users of the indirect method for turbulence measurement.

González-Rocha et al. (2019) characterize the frequency response of model-based wind estimation, but do not address hardware-dependent influences on turbulence measurements. Chen et al. (2026) apply measurement methods using the UAS as a sensor from laboratory tests to field measurements against meteorological masts, and find that differing payload mass and placement influence the relationship between attitude and wind speed, while leaving the characterization of turbulence unaddressed. Neumann and Bartholmai (2015) transfer measurements based on avionics data from the wind tunnel to the open field and validate them against reference sensors, but also do not investigate turbulence characteristics. Thielicke et al. (2021) and Schurig et al. (2026) take a similar approach by transferring their investigations from the wind tunnel to field measurements

https://doi.org/10.5194/egusphere-2026-4904
Preprint. Discussion started: 3 November 2026
© Author(s) 2026. CC BY 4.0 License.

and measuring around wind turbines, but use the direct measurement method without extending their analysis to the turbulence characteristics of the measured flow.

In this context, turbulence measurement is not limited to observations at individual measurement positions or to single-point statistics such as variance, as these may not be sufficient to fully characterize atmospheric properties for the intended use cases. Therefore, two-point turbulence statistics are employed. Here, the term *two-point* refers both to measurements at two spatially separated locations (using two sensors at two points in space) and to measurements obtained with a single sensor under Taylor's hypothesis, which relates temporal instances to spatial positions (conversion of lags between two points in time into distances between two points in space).

For example, Morales et al. (2011) show that the same single-point statistic can correspond to very different two-point statistics, as for example described by the probability density function (PDF). These statistics are particularly important in technical applications where wind loads need to be considered, for example in the design and operation of wind turbines. This highlights the importance of correctly describing such statistics. This is confirmed in the work by Schottler et al. (2017), which shows in a comparative wind tunnel study with an active grid that the same mean wind speed and turbulence intensity are insufficient to characterize a turbulent flow when evaluated for wind energy applications, as they do not provide information about intermittent or Gaussian inflow conditions. This motivates the development of a measurement system capable of providing accurate data for two-point statistics at the relevant scales. This point is reinforced by Schottler et al. (2018), who also demonstrate in a wind tunnel study that the wake behind a wind turbine is significantly wider when identified via two-point analysis. More generally, Kosović et al. (2026) investigate the research gaps and needs regarding the effects of atmospheric turbulence on wind turbine loads. Among other things, they identify the need to observe intermittent turbulence events.

The drones of the SWUF-3D fleet are intended to measure this non-Gaussianity or intermittency in the ABL and wake flows. Therefore, we verify whether the measured turbulence properties can reliably reflect those of reference sensors in time-increment analyses.

Since the SWUF-3D fleet also enables flexible, simultaneous, spatially distributed in situ measurements, it is now possible to conduct novel spatial multipoint analyses. Kistner et al. (2026) already evaluated multipoint measurements of vertical covariance, while Wetz et al. (2023) demonstrated that correlation and coherence can be analyzed over separation distances of 5–205 m using UAS fleets. Canter and Bailey (2019) report scale-dependent statistics based on velocity increments measured using fixed-wing UASs in forward flight. Kim et al. (2026) analyze velocity increments through second-order structure functions, but use measurements from a sonic anemometer mounted on an individual multicopter UAS.

However, increment analyses using drones as sensor have not yet been demonstrated, either at a single measurement position or across multiple positions.

Furthermore, the coherence analyses by Wetz et al. (2023) are based on the total horizontal wind, whereas Thedin et al. (2023) examine the coherence of the 3D wind components separately for different spatial separation directions using large-eddy simulations. Combining this analysis with drone-based coherence measurements opens up the possibility of flexible and omnidirectional multipoint analyses of turbulence in the ABL. Coherence depends on the velocity component under consideration and the spatial separation direction (Bowen et al., 1983; Krug et al., 2019; Thedin et al., 2023) and therefore, characterizing

https://doi.org/10.5194/egusphere-2026-4904
Preprint. Discussion started: 3 November 2026
© Author(s) 2026. CC BY 4.0 License.

turbulent structures of the three velocity components in all three spatial separation directions is relevant to boundary layer meteorology. Tong et al. (2026) perform a turbulence analysis using multipoint statistics derived from measurements. Among other things, they also use eight multicopter drones to measure the 3D velocity components using the indirect measurement method and compare them against an array of sonic anemometers. In doing so, they compare the wind speeds and the TKE derived from them. They do not perform an increment analysis or integrate the measurements from the various drones. A closely related study in the context of multipoint analysis is Sim et al. (2024), in which the authors analyze the distributions and correlations of wind speed increments using offshore data from multiple heights. They demonstrate simultaneous correlations of increments between two heights and show that increment PDFs are non-Gaussian at small scales but Gaussian at large scales. This demonstrates that multipoint spatial increment statistics provide meteorologically significant characterizations of the flow. However, the study is based on measurements taken with stationary anemometers, not with flexible systems such as drones.

In summary, there is no systematic identification of turbulence resolution limits for drones in wind tunnels or field measurements, no hardware comparison for turbulence measurements using the indirect method, no analysis of velocity increments based on indirect drone measurements, and no spatial intermittency analysis using multiple, spatially distributed multicopter drones in the available literature. These research gaps persist despite a general interest in higher-order statistical features of atmospheric turbulence. This gives rise to the following research questions:

1. What is the influence of hardware modifications to a UAS airframe on the turbulence resolution limits when using the indirect method?
2. What uncertainties arise in turbulence measurements using a single drone under laboratory conditions?
3. Can these uncertainties be confirmed in turbulence measurements from single drones under real-world conditions?
4. Do these constraints allow accurate turbulence analysis based on combined measurements from multiple drones under real-world conditions?

The aim of this work is therefore to identify the limits of turbulence resolution using different types of drone hardware, to verify accuracy under defined and reproducible flow conditions, and to validate these results using different drones under the same real-world flow conditions. Furthermore, using one hardware configuration as an example, we demonstrate how in situ fleet measurements can be used to measure the three wind components at spatially distributed positions to determine coherence and quantify the non-Gaussianity of small-scale turbulence.

The next section describes the multicopter UAS used, including the hardware modifications, the wind tunnel with an active grid and reference sensors, and the experimental setup at a research wind farm. Section 3 addresses the methods for identifying measurement limits and for verifying and validating the 3D turbulence measurements. This includes the respective calculations of key parameters for characterizing turbulence and error metrics. The results are then presented in Sect. 4 and discussed in Sect. 5 and 6.

https://doi.org/10.5194/egusphere-2026-4904
Preprint. Discussion started: 3 November 2026
© Author(s) 2026. CC BY 4.0 License.

2 System description and Experimental Setup

2.1 Uncrewed Aerial Systems

Within the SWUF-3D fleet, the basic hardware, based on the QAV250 airframe from Holybro (Fig. 1), can be modified in various ways. First, since the work of Wildmann and György (2025), we have been using $5.5''$ propellers instead of $5.0''$ propellers for the fleet. Furthermore, we achieve longer flight times with newer battery generations: our first step here was switching from 3500 mAh LiPo batteries to 4500 mAh LiIo batteries. Since our wind measurements are based on accelerometer data, which are influenced by the airframe's vibrations, we investigate how mounting the autopilot on foam pads to damp these vibrations affects the measurement behavior for turbulence. All drone configurations examined in this study and their specifications are listed in Table 1. We operate all drones using a custom version of the PX4 v14.1 operating system on the Pixhawk 4 Mini autopilot. To maintain the drone's position in hover flight, we use GNSS and a barometer in field measurements, and the MTF-01 optical flow sensor and rangefinder module from RoboFusion in the wind tunnel.

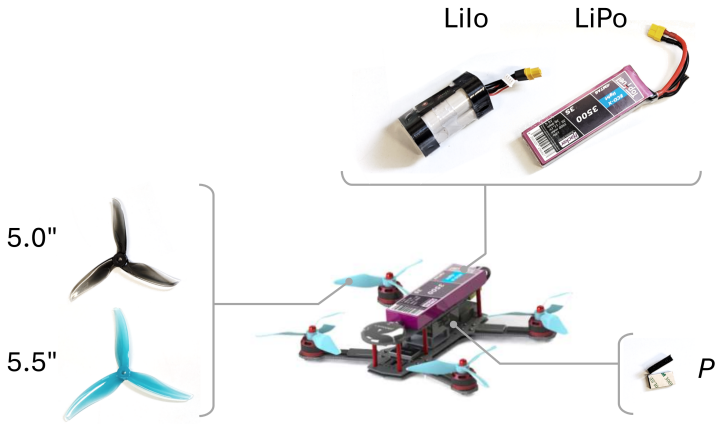


Figure 1. The QAV250 drone with its various modified hardware components (adapted from Hofmann, 2025).

Table 1. System description of the used UAS configurations.

Parameter	$5.5''$ LiPo	$5.5''$ LiIo	$5.0''$ LiPo	$5.5''$ LiPo P
Battery type	3500 mAh LiPo	4500 mAh LiIo	3500 mAh LiPo	3500 mAh LiPo
Weight (including battery)	0.655 kg	0.665 kg	0.655 kg	0.655 kg
Propeller size	$5.5''$	$5.5''$	$5.0''$	$5.5''$
Max. flight time	20 min	27 min	15 min	20 min

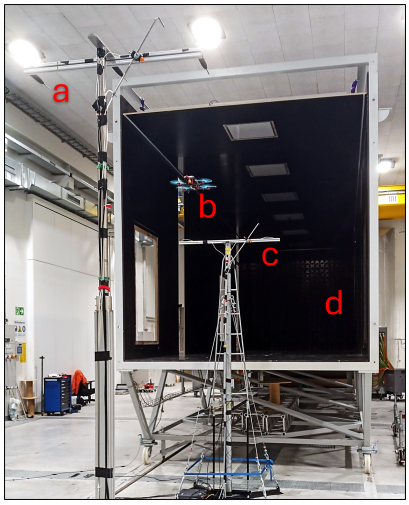
https://doi.org/10.5194/egusphere-2026-4904
Preprint. Discussion started: 3 November 2026
© Author(s) 2026. CC BY 4.0 License.

2.2 Wind tunnel

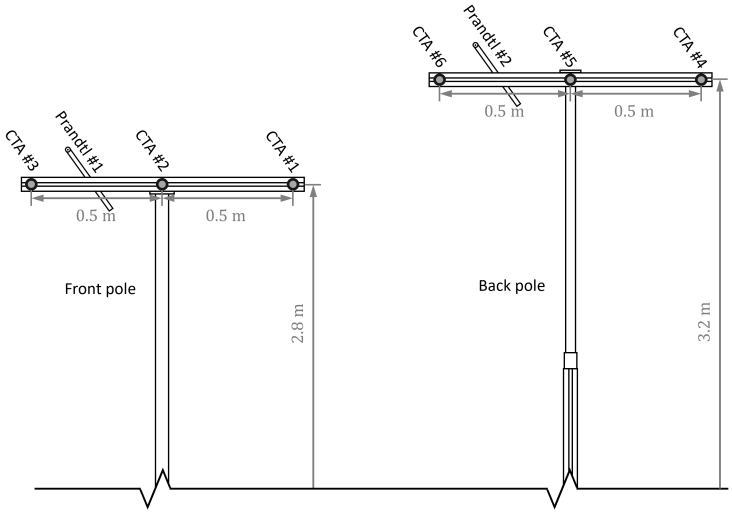
The measurements were conducted in the large ForWind wind tunnel of the University of Oldenburg, featuring a $3\ \mathrm{m} \times 3\ \mathrm{m}$ test section equipped with an active grid composed of 80 independent shafts for turbulence generation (Kröger et al., 2018; Neuhaus et al., 2021). In previous tests in the same wind tunnel (Kistner et al., 2024), we used the open test section setup and placed a drone 2.5 m downstream of the grid. This allowed us to measure the response of our drone to various inflows, including gusts and flows with different turbulence levels. However, due to the open test section setup and active grid motion protocols used, overly energetic fluctuations around the drone's potential maximum resolution frequency were measured, as the flow acted like a jet. This constrained our ability to investigate the limits of turbulence measurements. To mitigate this effect, but to still ensure safe flight of the UAS in the flow, we selected a semi-closed measurement section setup for this study (see Fig. 2a). Two movable section elements, each 6 m long, were placed at the inlet of the wind tunnel, and a new measurement rig was positioned at the outlet of the second test section. The 12 m long closed test section contained the flow generated by the active grid and was sufficiently long to ensure a fully homogeneous flow. Compared to the open test section (without any elements), the flow exiting the closed section was more stable. This setup allowed us to remove the high spectral content in the flow at the frequency range of interest, where we placed our reference measurements and the drone.

The reference sensors used to measure turbulence were 1D hot-wire sensors connected to multichannel constant-temperature anemometers (CTAs) from Dantec Dynamics (54N80-CTA). These sensors were attached to two system profiles mounted on a front pole and a back pole, respectively (see Fig. 2b). The hot-wires were calibrated against Prandtl probes on each measurement day, during which the temperature remained constant, with variations lower than 0.5°C. The hot-wires were arranged to span the measurement volume in which the drone moved, without disturbing the flow measured by the drone or vice versa. This is based on the observations of Kistner et al. (2024), as the drone's downwash strongly affected the hot-wires mounted behind it at flight height and below. To reduce this effect, three sensors were mounted along a horizontal line with a spacing of 0.5 m between sensors and in front of the drone at a height of 2.8 m from the ground (1.3 m from the wind tunnel floor). Behind the drone, 3.7 m behind the front pole, three additional sensors were mounted at a height of 3.2 m from the ground (1.8 m from the wind tunnel floor), while the drone hovered between them at a height of 3.0 m. Thus, a total of six hot-wires were used, measuring wind speed time series with a sampling frequency of 1000 Hz.

https://doi.org/10.5194/egusphere-2026-4904
Preprint. Discussion started: 3 November 2026
© Author(s) 2026. CC BY 4.0 License.



(a) Measurement setup in the wind tunnel with a) reference sensors on the back pole, b) UAS hovering at a height of 3.0 m, c) reference sensors on the front pole, and d) active grid at the outlet.



(b) Schematic representation of the front view of the reference sensor poles with the positions of the CTAs and Prandtl probes.

Figure 2. Experimental setup in the wind tunnel for measurements of statistically reproducible turbulence.

2.3 Wind park

To validate turbulence measurements using various UAS configurations under real-world conditions, we use the measurement mast array located at the DLR WiValdi research wind farm. This array consists of three meteorological masts, each spaced 50 m apart and oriented along a geographical azimuth direction of 10°–190°. These masts are 100 m or 150 m high and are equipped with various anemometers. Selected 3D sonic anemometers from Thies Clima at heights of 20 m, 25 m, 90 m, and 100 m serve as reference sensors for the drone measurements.

https://doi.org/10.5194/egusphere-2026-4904
Preprint. Discussion started: 3 November 2026
© Author(s) 2026. CC BY 4.0 License.

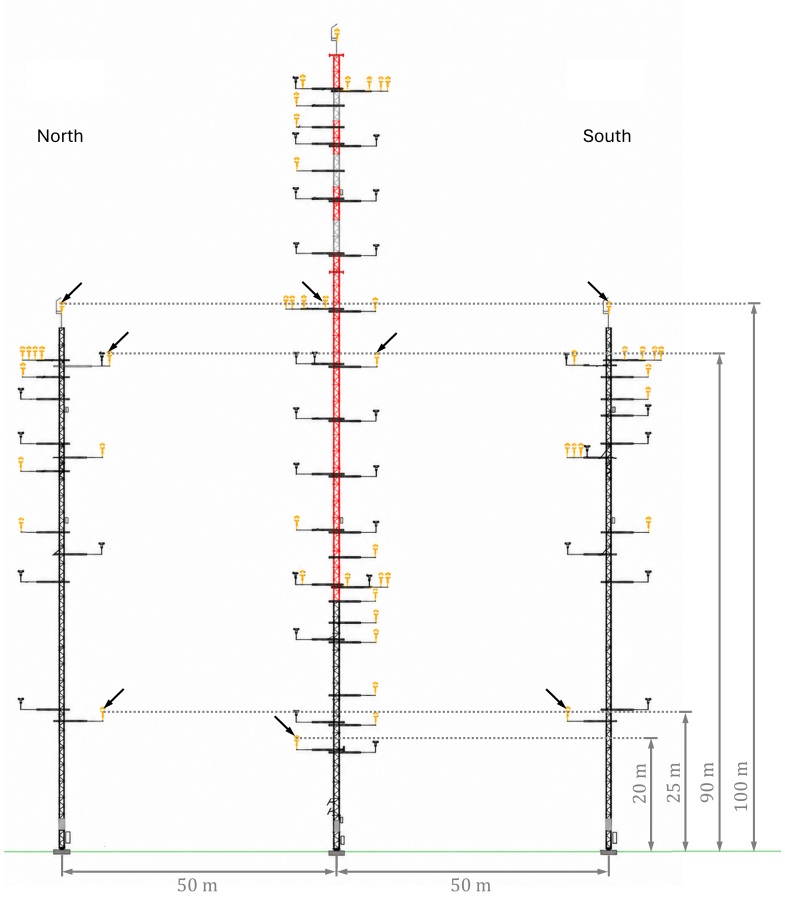
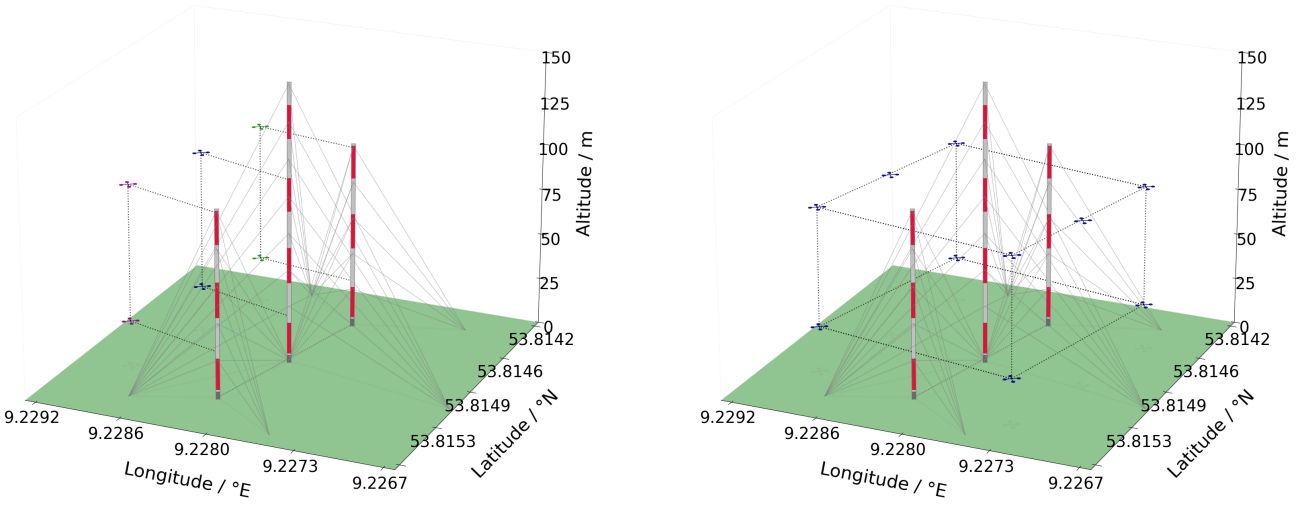


Figure 3. Schematic representation of the west view of the measurement mast array, with sonic anemometers shown in orange and cup anemometers shown in black. The sonic anemometers selected as references at heights of 20, 25, 90, and 100 m are indicated by the black arrows.

We conduct the validations using the $5.5''$ LiPo, $5.5''$ LiIo, and $5.0''$ LiPo configurations. This involves two flight patterns, which we carried out during measurement campaigns in July 2024 and March 2025. One pattern is the configuration comparison flight pattern for a direct comparison of the three QAV250 configurations in the same airflow (see Fig. 4a), an the other pattern is the box-shaped flight pattern utilizing exclusively one QAV250 configuration (see Fig. 4b).

https://doi.org/10.5194/egusphere-2026-4904
Preprint. Discussion started: 3 November 2026
© Author(s) 2026. CC BY 4.0 License.



(a) Configuration comparison flight pattern

(b) Box-shaped flight pattern

Figure 4. Experimental setup for the validation measurements around the measurement mast array. The dashed black lines represent the orientations of the drones relative to each other and to the reference sensors on the masts.

In the configuration comparison pattern two UASs of the same configuration hover one above the other at heights of 25 m and 100 m and at a horizontal distance of 50 m from the reference sensors. To compensate for local or sensor effects, we swapped the positions of the upper and lower UASs, the UAS pairs relative to each other, and the fleet positions west and east of the masts. In total, we conducted 13 fleet flights, from which 70 usable time series with an average duration of 9.8 minutes were obtained. A more detailed overview of the individual flights can be found in Table E1.

As mentioned above, characterizing turbulent structures of the three velocity components for all three spatial separation directions is relevant to atmospheric studies. Thus, the box-shaped flight pattern, which was already employed for the analyses in Kistner et al. (2026), is used. This pattern consists of 10 drones in the $5.5''$ LiPo configuration only, which at that time served as the standard configuration for the SWUF-3D fleet. In this pattern, the drones hover simultaneously at distances of 50 m upstream and downstream of the measurement mast array at altitudes of 25 m and 90 m, thereby providing separations in all three spatial directions and enclosing a box-shaped volume around the array. We conducted 17 fleet flights, resulting in 85 usable time series with an average duration of 11.1 minutes. For a more detailed overview of the individual flights, see Table E2.

https://doi.org/10.5194/egusphere-2026-4904
Preprint. Discussion started: 3 November 2026
© Author(s) 2026. CC BY 4.0 License.

3 Methods

Our wind measurement is based on the post-processing of the drone's logged avionics data during hover flight. Using 3D acceleration data, Euler angles, magnetometer measurements, and motor control signals, we can determine the speed and direction of the wind acting on the drone as it maintains its position by adjusting thrust and tilt. The methods for the wind algorithm and how the calibration coefficients are determined are described in detail in Kistner et al. (2024, 2026). The acceleration data logged by the autopilot are measured at a resolution of up to 250 Hz. At this sampling rate, the data contain not only the drone's acceleration caused by turbulence it encounters, but also the accelerations caused by mechanical vibrations of the drone itself (see Fig. 5). To prevent these signals from being incorrectly interpreted as turbulence information, we filter them out of the acceleration data before converting the data into wind speeds. Therefore, we downsample the avionics data to a suitable frequency f_s. To prevent aliasing effects, we apply a second-order Butterworth filter with a cutoff frequency f_c before downsampling.

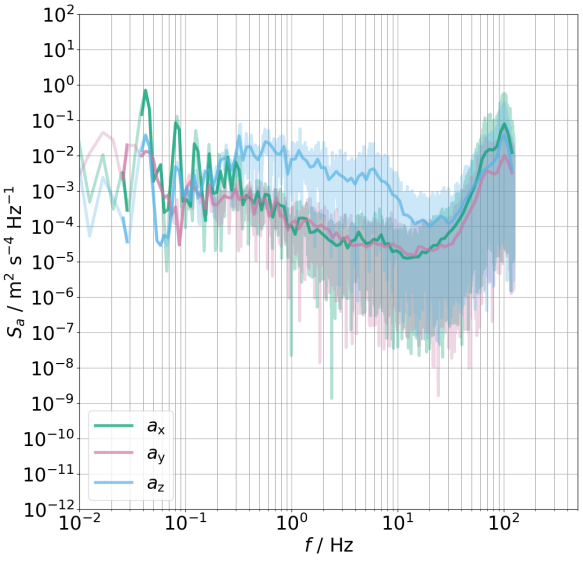


Figure 5. Power spectral density of the 3D acceleration components in the drone's body-fixed coordinate system under low turbulent wind conditions with wind speeds ranging from 0 to 18 $\mathrm{m\,s^{-1}}$. The green curve represents the longitudinal accelerations, the magenta curve the lateral accelerations, and the blue curve the vertical accelerations. While the curves initially decrease with increasing frequency, a significant increase is observed at high frequencies, caused by accelerations due to mechanical vibrations of the drone.

The analysis in this work starts by determining the usable spectral frequency range of each drone. From this, f_s and f_c are derived for generating low-noise wind speed time series. Based on these processed wind time series, turbulence statistics of temporal velocity increments under laboratory and field conditions are evaluated against reference measurements and compared

https://doi.org/10.5194/egusphere-2026-4904
Preprint. Discussion started: 3 November 2026
© Author(s) 2026. CC BY 4.0 License.



across different UAS hardware. The analysis is then extended to multi-sensor analysis from fleet measurements using spatial velocity increments and coherence to assess the spatial turbulence structure.

This analytical workflow can be summarized as follows: (1) determination of filter coefficients, (2) single-drone uncertainty estimation in the wind tunnel, (3) single-drone uncertainty validation in the field, and (4) multi-drone spatial turbulence validation in the field.

3.1 Wind tunnel

Prior to verification and validation, we perform the calibration of the measurement of the 3D wind components for all hardware configurations using the methods described in Kistner et al. (2024, 2026), by conducting test flights with reference sensors in the open test section. The resulting accuracies of the wind speed measurements are listed in Table E4.

3.1.1 Identification of turbulence resolution limits

When selecting the sampling frequency f_s for all configurations, two objectives apply: first, to ensure that high-frequency noise is filtered out, and second, to sample the highest possible frequency range to capture the small-scale features of turbulence. We proceed in two steps: first, we examine the drone's 3D accelerations in the measurement setup used for calibration at wind speeds that are incrementally increased from 0 to 18 $\mathrm{m\,s^{-1}}$ under laminar conditions. We analyze the scale-dependent distribution of fluctuations via the one-sided power spectral density (PSD) S of the accelerations in its bin-averaged form $\overline{S}$ to qualitatively identify the frequency above which noise dominates the acceleration signal. For the averaging, we determine the bins using the Freedman–Diaconis rule (Freedman and Diaconis, 1981) and the interquartile range (IQR), which is explained in more detail in Appendix A. In the second step of the analysis, we conduct measurements using the drones in turbulent flows generated by the active grid and process the data using the qualitatively identified maximum frequency.

Fig. 5 shows the PSD of the three acceleration directions for an example flight. From this, we can already qualitatively determine that noise clearly dominates at approximately 12.5 Hz. In accordance with the Nyquist theorem (Nyquist, 1924), we use the doubled value of this frequency and set 25 Hz as f_s for the first analysis step.

In the second step, similar to Kistner et al. (2024), we use the same protocols and one additional protocol to generate turbulence at different mean wind speeds (see Table E3), while performing the measurements in the experimental setup described in Sect. 2.2. By doing so, we increase the PSD of the wind speed and thus also its variance. We compare the bin-averaged spectra derived from the UAS measurements with those from the reference measurements and determine the frequency at which the UAS spectra begin to deviate from the reference spectra. Using this approach, we can determine the maximum frequencies of the UAS measurements as a function of variance. Since the drone moves within the measurement volume defined by the six reference CTAs, we do not use a single CTA as a reference, but instead construct the reference spectrum $\overline{S}_\mathrm{ref}$ from them:

$$\bar{S}_\mathrm{ref}(j) = \frac{1}{6}\sum_{i=1}^{6} \bar{S}_{\mathrm{CTA},i}(j), \qquad j = 0,\ldots,B-1 \tag{1}$$

https://doi.org/10.5194/egusphere-2026-4904
Preprint. Discussion started: 3 November 2026
© Author(s) 2026. CC BY 4.0 License.

where $(\bar{f}_{\mathrm{CTA},i}, \bar{S}_{\mathrm{CTA},i})$ denotes the binned spectra of the $i = 1, \ldots, 6$ reference CTAs and j denotes the bin index in the number of bins B. To compare the averaged spectrum derived from UAS measurements, $\bar{S}_{\mathrm{UAS}}$, with $\bar{S}_{\mathrm{ref}}$ on a common grid, both spectra are interpolated onto a shared frequency axis f^* derived from the binned frequency vectors, yielding $\bar{S}^{\mathrm{int}}_{\mathrm{UAS}}(f^*)$ and $\bar{S}^{\mathrm{int}}_{\mathrm{ref}}(f^*)$. The comparison is restricted to the common frequency band up to the highest UAS frequency. We use the commonly applied 3 dB criterion as the threshold for a significant spectral deviation, which is expressed as a factor-of-two constraint on the PSD ratio as

$$\frac{1}{2} < \frac{\bar{S}^{\mathrm{int}}_{\mathrm{ref}}(f^*)}{\bar{S}^{\mathrm{int}}_{\mathrm{UAS}}(f^*)} < 2. \tag{2}$$

The divergence frequency $f_{\max}$ is defined as the highest frequency in the analysis band for which the ratio in Eq. (2) remains within the 3 dB limits (Fig. 6). The corresponding spectral level is reported as

$$S_{\min} = \bar{S}^{\mathrm{int}}_{\mathrm{ref}}(f_{\max}). \tag{3}$$

We then set $f_{\mathrm{s}} = 2 f_{\max}$ using the highest $f_{\max}$ achieved by the respective UAS. To avoid aliasing effects while also avoiding distortion of the analyzed spectrum below f_{s}, we set $f_{\mathrm{c}} = 0.75 f_{\max}$.

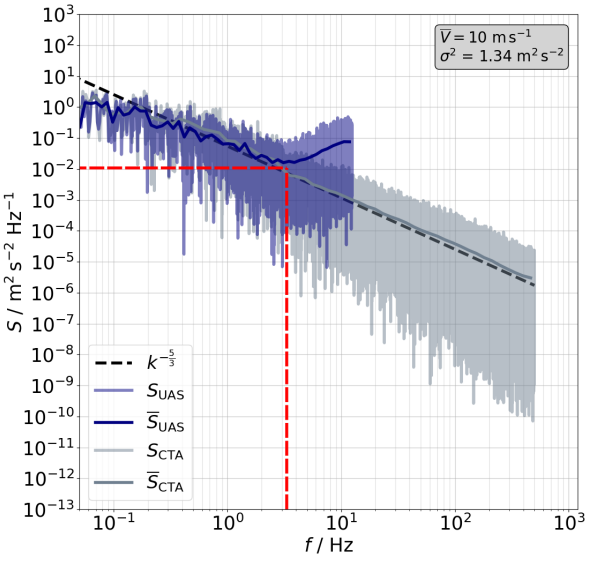


Figure 6. Example comparison of the power spectral densities S obtained from UAS and reference measurements in the wind tunnel, together with their bin-averaged counterparts $\overline{S}$. The blue curves represent the (bin-averaged) spectra derived from the UAS measurements, and the grey curves represent the (bin-averaged) spectra derived from the reference measurements. The dashed red lines indicate the respective $S_{\min}$ at the last frequency $f_{\max}$ at which the deviations of the bin-averaged spectra remain below 3 dB. The dashed black line represents a spectrum following the Kolmogorov $-5/3$ power law.

https://doi.org/10.5194/egusphere-2026-4904
Preprint. Discussion started: 3 November 2026
© Author(s) 2026. CC BY 4.0 License.



3.1.2 Verification of turbulence retrieval

Using the new f_s and f_c, we reprocess the UAS measurement data from the test flights in turbulent flows and derive the wind speed V from the reprocessed data. After checking that the mean wind speed is reproduced correctly, we focus on retrieval of turbulence quantities and first determine the wind speed variance σ^2 as a single-point turbulence statistic, since it is a measure of the absolute intensity of wind speed fluctuations.

The agreement between UAS and reference measurements of wind speed variance over N time series is quantified using the root mean square error (RMSE), defined as

$$\varepsilon_{\sigma^2} = \sqrt{\frac{1}{N}\sum_{i=1}^{N}\left(\sigma^2_{\mathrm{UAS},i} - \sigma^2_{\mathrm{ref},i}\right)^2}. \tag{4}$$

As a relative measure of error, the RMSE is normalized by the mean of the reference values, resulting in the normalized root mean square error (nRMSE):

$$\varepsilon^*_{\sigma^2} = \frac{\sqrt{\frac{1}{N}\sum_{i=1}^{N}\left(\sigma^2_{\mathrm{UAS},i} - \sigma^2_{\mathrm{ref},i}\right)^2}}{\frac{1}{N}\sum_{i=1}^{N}\sigma^2_{\mathrm{ref},i}}. \tag{5}$$

Compared to the reference sensors, we then obtain an absolute error value for each UAS configuration based on the error metrics as a benchmark for measurement accuracy under laboratory conditions, and use these error values to compare the different UAS hardware configurations with one another. As shown by Schottler et al. (2017, 2018), two-point statistics are required in addition to single-point statistics, since the latter alone are insufficient for characterizing turbulence. Therefore, we perform a statistical analysis of velocity increments based on the measured wind speed time series. For a wind speed time series $V(t)$, temporal velocity increments are defined as

$$\delta V_\tau(t) = V(t+\tau) - V(t), \tag{6}$$

where τ denotes the time lag between two values in the time series. For discretely sampled data, $\tau = k f_s^{-1}$, where k is the lag in sampling intervals. The corresponding normalized temporal increments are

$$\delta\tilde{V}_\tau(t) = \frac{\delta V_\tau(t) - \overline{\delta V_\tau}}{\sigma_{\delta V_\tau}}, \tag{7}$$

where $\overline{\delta V_\tau}$ and $\sigma_{\delta V_\tau}$ are determined separately for each time lag τ.

For a weakly stationary time series, the increment variance is related to the autocovariance $C_V(\tau)$ according to

$$\sigma^2_{\delta V_\tau} = 2\left[C_V(0) - C_V(\tau)\right]. \tag{8}$$

It therefore represents a second-order two-point statistic. Through the Wiener–Khinchin theorem (Pope, 2000), which relates the autocovariance function to the PSD, the scale dependence of $\sigma^2_{\delta V_\tau}$ is also directly linked to the spectral energy distribution. Normalization by $\sigma_{\delta V_\tau}$ separates this second-order amplitude variation from changes in the shape of the increment distribution.

https://doi.org/10.5194/egusphere-2026-4904
Preprint. Discussion started: 3 November 2026
© Author(s) 2026. CC BY 4.0 License.

This normalization allows the comparison of distribution shapes regardless of the variance of the increments. For each time lag τ, the increments form a separate time series, from which the statistical moments and PDFs, denoted by p, are determined. The PDFs of the normalized increments and their higher standardized moments can be used to investigate higher-order two-point statistics and intermittent, non-Gaussian fluctuations. The time lag can also be expressed as a spatial separation r under the assumption of Taylor's frozen turbulence hypothesis (Taylor, 1938), with $r = \tau \overline{V}$. Deviations from Gaussianity are quantified in both temporal and spatial increment analyses using the kurtosis κ as the fourth standardized moment of the normalized increments:

$$\kappa = \overline{(\delta\tilde{V})^4}. \tag{9}$$

Here, $\delta\tilde{V}$ denotes the normalized increments, and the overbar denotes the average over all increments of the respective time lag or separation distance. The kurtosis is not the excess kurtosis and therefore, for a Gaussian distribution, $\kappa = 3$. The PDFs of $\delta\tilde{V}_\tau$ are estimated using normalized histograms, with the number of bin widths determined using the Freedman–Diaconis rule (Freedman and Diaconis, 1981). The Gaussian normal density serves as the reference distribution:

$$p_{\text{Gauss}}(\delta\tilde{V}_\tau) = \frac{1}{\sqrt{2\pi}} e^{-\frac{1}{2}(\delta\tilde{V}_\tau)^2}. \tag{10}$$

Furthermore, we compare the PDFs determined from the time series measured using UASs and CTAs to assess the drone's capabilities for identifying intermittency in turbulent flows. A good indicator of this is the analysis of κ across different τ values. We also perform this analysis using only the CTAs, without any UAS flying in the flow. Since the CTAs sample at up to 1000 Hz, significantly shorter τ values can be examined, allowing us to analyze the flow beyond the measurement limits of the UASs. This reveals which properties of the flow are not captured. Given that the UAS measurements have limited resolution and duration, extreme deviations from Gaussianity are less likely to be captured. To still provide modelers in wind turbine engineering with an estimate of intermittency based on our measurements, we fit a Castaing distribution (Castaing et al., 1990) to the increment PDFs, following a commonly used approach that has been shown empirically to perform well (Böttcher et al., 2006; Wächter et al., 2012; Schottler et al., 2017).

Rather than characterizing intermittency only through an individual standardized moment such as the kurtosis, this approach provides a parametric representation of the entire increment PDF. The kurtosis summarizes the fourth-order tail weight of a distribution but does not uniquely determine its shape, while a fitted PDF allows probabilities of arbitrary increment amplitudes and their probabilities to be evaluated within the assumptions of the model. This is particularly relevant for intermittent data, for which empirical characterizations are strongly influenced by rare events. This Castaing model describes the PDF of the velocity increments as a superposition of Gaussian distributions with different widths. For the normalized increments $\delta\tilde{V}_\tau$, we write the Castaing PDF as

$$p_{\text{Castaing}}(\delta\tilde{V}_\tau, \Lambda^2) = \frac{1}{2\pi\Lambda} \int_0^\infty \frac{1}{\sigma_{\text{G}}^2} \exp\left[-\frac{(\delta\tilde{V}_\tau)^2}{2\sigma_{\text{G}}^2}\right] \exp\left[-\frac{\ln^2(\sigma_{\text{G}}/\sigma_{\text{G},0})}{2\Lambda^2}\right] \mathrm{d}\sigma_{\text{G}}. \tag{11}$$

Here, σ_{G} denotes the dimensionless width of the Gaussian subdistributions within the Castaing model, while $\sigma_{\text{G},0}$ denotes the reference value of the lognormally distributed Gaussian widths. The shape factor Λ^2 denotes the variance of the logarithmic

https://doi.org/10.5194/egusphere-2026-4904
Preprint. Discussion started: 3 November 2026
© Author(s) 2026. CC BY 4.0 License.

width distribution and therefore quantifies the deviation from a Gaussian distribution. It is calculated from the kurtosis (Chillà et al., 1996):

$$\Lambda^2 = \frac{\ln(\kappa/3)}{4}. \tag{12}$$

Accordingly, when $\Lambda^2 = 0$, the distribution is Gaussian.

3.2 Wind park

For the validation of the uncertainties determined in the wind tunnel, we first quantify uncertainty associated with measurements using individual drones, and then the uncertainties in the analysis of multipoint measurements obtained using multiple drones. To do this, we use the wind tunnel calibrations for the various UAS configurations and process the measurement data using the f_s and f_c values determined in the wind tunnel.

3.2.1 Validation of turbulence retrieval with different drone configurations

To validate the measurement uncertainties of individual drones, we conduct measurements using the configuration comparison pattern (Fig. 4a). In this process, we compare the statistical turbulence parameters derived from the wind speed time series measured by the UASs with those derived from the corresponding reference sensors. Here, we analyze the measurements obtained with the drone configurations, excluding the configuration with foam pads. For our accelerometer-based wind measurements, determining an offset is necessary (Wetz and Wildmann, 2022). The foam pads make the autopilot module movable relative to the airframe, causing the offset to shift continuously. Since the wind measurement is sensitive to this offset, field measurements with drones equipped with foam pads are not practical for us. The limited flight time of the drones restricts the measurement intervals over which we can compare the sonic measurements with the drone measurements. Unlike wind tunnel measurements, field measurements of finite duration can typically only approximately satisfy the assumption of local stationarity, as meteorological boundary conditions are always variable to some extent. This is significant because we analyse the kurtosis, which is particularly sensitive to rare extreme increments or outliers. Therefore, when comparing the two-point statistics derived from drone and sonic measurements, we estimate the intrinsic uncertainty of the kurtosis to distinguish the natural statistical variation in the reference measurements caused by a finite sample size from actual sensor-related deviations between UASs and sonics.

To estimate the intrinsic uncertainty of the kurtosis derived from the reference sensors, we use a bootstrapping approach similar to that described by Laubrich et al. (2008). To do this, starting from the middle of the analyzed time series, we symmetrically extend the measurement duration under investigation by a factor of three to approximately 30 min. This is possible because continuous measurement data are available from the reference sensors. We divide these data into three blocks of equal length and calculate the kurtosis for each block separately according to Eq. (9), and then average these values:

$$\overline{\kappa}(\tau) = \frac{1}{3}\sum_{j=1}^{3}\kappa_j(\tau), \qquad j = 1,2,3\,. \tag{13}$$

https://doi.org/10.5194/egusphere-2026-4904
Preprint. Discussion started: 3 November 2026
© Author(s) 2026. CC BY 4.0 License.

The intrinsic uncertainty of the kurtosis is derived from the standard deviation of the three block-wise kurtosis values and is evaluated for the respective time lag τ:

$$\sigma_{\kappa,\mathrm{int}}(\tau) = \sqrt{\frac{1}{2}\sum_{j=1}^{3}\left(\kappa_j(\tau) - \overline{\kappa}(\tau)\right)^2}. \tag{14}$$

Analogously to the nRMSE, we also express the intrinsic uncertainty as a relative quantity in order to be able to compare the nRMSE values determined for the drone measurements with the sonic measurements. For this purpose, we normalize the intrinsic uncertainty in the same way as the RMSE (Eq. (5)) by dividing it by the kurtosis of the original reference interval:

$$\varepsilon^*_{\kappa,\mathrm{ref}}(\tau) = \frac{\sigma_{\kappa,\mathrm{int}}(\tau)}{\kappa_{\mathrm{ref}}(\tau)}. \tag{15}$$

The quantity $\varepsilon^*_{\kappa,\mathrm{int}}$ thus describes the normalized intrinsic uncertainty of the reference kurtosis for the corresponding τ.

3.2.2 Validation of turbulence retrieval with drone fleet measurements

To obtain more accurate statistics based on a larger number of measurement points and fleet flights, we use the box-shaped pattern with the $5.5''$ LiPo configuration and validate the turbulence measurements over several measurement locations. This flight pattern allows for simultaneous and spatially distributed turbulence measurements in all three spatial directions. Given the prevailing wind directions in the measurement data, we perform the analyses based on the lateral and vertical directions within the pattern, as the parallel alignment with the measurement mast array enables us to directly compare the UAS measurements with the reference measurements. In doing so, we analyze the statistics of the spatial velocity increments for the sensor pairs from the UASs and sonic anemometers, respectively. For two synchronously sampled wind speed signals at two positions x and $x+r$, the spatial velocity increments are defined as

$$\delta V_r(t) = V(x+r,t) - V(x,t) = V_2(t) - V_1(t), \tag{16}$$

where r denotes the separation distance between the sensors. The corresponding normalized spatial increments are

$$\delta\tilde{V}_r(t) = \frac{\delta V_r(t) - \overline{\delta V_r}}{\sigma_{\delta V_r}}, \tag{17}$$

where $\overline{\delta V_r}$ and $\sigma_{\delta V_r}$ are determined separately for each separation distance $r = |r|$.

Note that in the spatial increment analyses, the three wind components of V are examined separately in order to specifically utilize the additional directional information provided by the 3D measurement for characterizing longitudinal, lateral, and vertical turbulence structures. The horizontal wind components are transformed into a flow-oriented coordinate system along the mean wind direction. Note that u, v, and w denote the longitudinal, lateral, and vertical wind components within this flow-oriented coordinate system. Each of Eqs. (9), (11), (12), (16), and (17) is applied separately to the three velocity components u, v, and w. Since we positioned only two UASs above each other in the vertical direction and three UASs side by side in the lateral direction relative to the main wind direction, only one and two spatial lags, respectively, are available for the increment analysis.

https://doi.org/10.5194/egusphere-2026-4904
Preprint. Discussion started: 3 November 2026
© Author(s) 2026. CC BY 4.0 License.

To quantify the frequency-dependent coupling of turbulence between two measurement points, we apply coherence analysis to the same sensor pairings. This allows us to determine the extent to which two spatially separated measurements capture common turbulent fluctuations. For this, we use the vertically separated sensor pairs with a separation of 65 m and the laterally distributed sensor pairs at two distances, with separations of approximately 50 m and 100 m. For each velocity component, the magnitude-squared coherence γ^2 between two signals is calculated as

$$\gamma^2_{VV}(f) = \frac{|S_{V_1V_2}(f)|^2}{S_{V_1V_1}(f)\,S_{V_2V_2}(f)}. \tag{18}$$

Here, $S_{V_1V_2}(f)$ denotes the cross power spectral density, and $S_{V_1V_1}(f)$ and $S_{V_2V_2}(f)$ denote the corresponding auto power spectral densities. For each sensor configuration and each wind speed component, the coherence is first determined separately for each measurement flight, for the UASs and sonics, respectively. This yields a set of N coherence estimates $\gamma_i^2(f)$ as a function of frequency f. To obtain a statistically reliable assessment of the typical agreement between drone and reference measurements, we compute the median coherence from these estimates separately for each frequency across all measurement flights. For each frequency f, the coherence values of the individual measurements are first defined as

$$\gamma_i^2(f), \qquad i = 1, \ldots, N \tag{19}$$

and then sorted by magnitude:

$$\gamma^2_{i\,(1)}(f) \le \gamma^2_{i\,(2)}(f) \le \cdots \le \gamma^2_{i\,(N)}(f). \tag{20}$$

Here, $\gamma^2_{i\,(k)}(f)$ denotes the kth-smallest coherence value at frequency f. The representative coherence is then calculated as the median of these sorted values:

$$\widetilde{\gamma^2}(f) = \begin{cases} \gamma^2_{i\,(\frac{N+1}{2})}(f), & \text{for odd } N, \\ \dfrac{1}{2}\left[\gamma^2_{i\,(\frac{N}{2})}(f) + \gamma^2_{i\,(\frac{N}{2}+1)}(f)\right], & \text{for even } N. \end{cases} \tag{21}$$

4 Results

4.1 Identification of turbulence resolution limits

Based on the wind tunnel tests and avionics data processing at $f_\mathrm{s} = 25$ Hz, we were able to determine the respective f_max values as a function of the flow variance for the various UAS configurations. These are shown in Fig. 7:

https://doi.org/10.5194/egusphere-2026-4904
Preprint. Discussion started: 3 November 2026
© Author(s) 2026. CC BY 4.0 License.

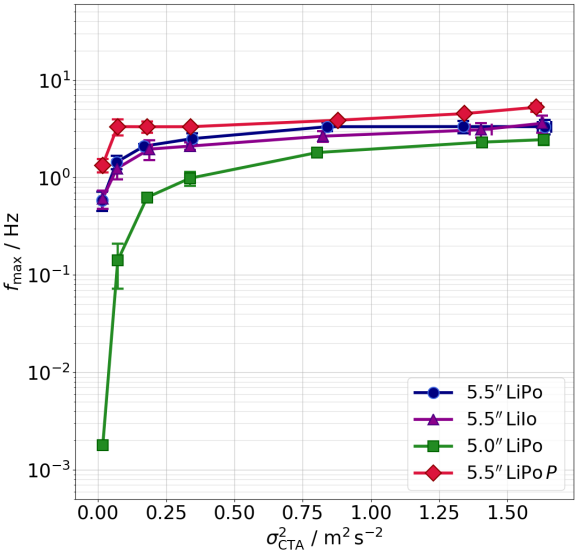


Figure 7. Comparison of the highest frequencies $f_{\max}$ that can be resolved with different UAS configurations at different levels of wind speed variance σ^2. The blue curve represents the data for our standard QAV250 configuration, while the other curves represent data from modified configurations based on it, with changes of the battery (purple), the propellers (green), and the autopilot mounting (red). The vertical error bars show the standard deviation between the maximum frequencies achieved using the six individual spectra from the CTAs. The horizontal error bars show the reproducibility when the data point is based on multiple drone measurements.

The comparison of the different UAS configurations (Fig. 7) shows a high degree of agreement between the $5.5''$ LiPo and $5.5''$ LiIo configurations, with resolvable frequencies of up to approximately 3.5 Hz and largely similar behavior across the entire measurement range. Across the entire measurement range, the $5.5''$ LiPo P configuration has the highest resolvable frequencies, up to approximately 5.0 Hz, whereas the $5.0''$ LiPo configuration has the lowest maximum resolvable frequency, with a maximum of about 2.5 Hz. This difference is particularly significant for the $5.0''$ LiPo configuration, as turbulence at low frequencies is resolved significantly less well for this configuration. The trend of the smallest achievable PSDs as a function of variance is shown in Fig. B1.

4.2 Verification of turbulence retrieval

Based on the wind tunnel tests and the data processing using $f_{\mathrm{s}} = \max(f_{\max})$ for the respective UAS configurations, we can compare the variance determined from the UAS measurements with that determined from the reference measurements:

https://doi.org/10.5194/egusphere-2026-4904
Preprint. Discussion started: 3 November 2026
© Author(s) 2026. CC BY 4.0 License.

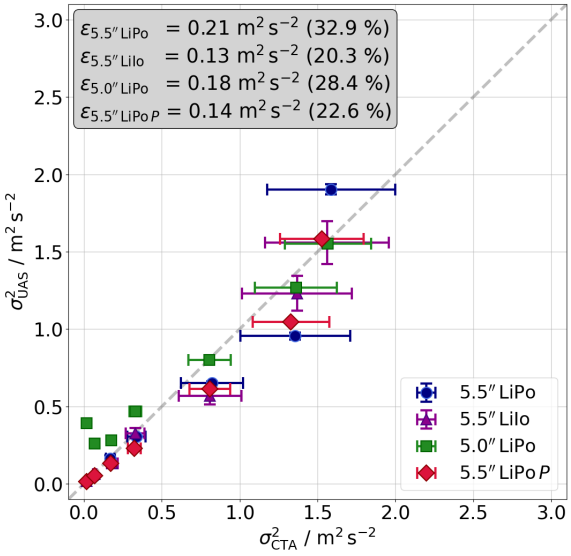


Figure 8. Comparison of the variances σ^2 of wind speeds determined from wind tunnel measurements with different UAS configurations against the CTAs. The blue markers represent the data for our standard QAV250 configuration, while the other markers represent data from modified configurations based on it, with changes of the battery (purple), the propellers (green), and the autopilot mounting (red). The horizontal error bars show the standard deviation between the variances derived from the six reference CTAs. The vertical error bars show the reproducibility when the data point is based on multiple drone measurements.

The $5.5''$ LiPo configuration shows the highest RMSE among the configurations, with a value of $0.21\ \mathrm{m^2\,s^{-2}}$ (Fig. 7), while the RMSE values of the other configurations remain below $0.2\ \mathrm{m^2\,s^{-2}}$. The overestimation of low variances in the $5.0''$ LiPo measurements is notable. The errorbars for the reference values are discussed in Sec. 5.

The frequency limits identified in Sect. 4.1, in combination with the high-resolution reference measurements obtained with CTAs in the wind tunnel, allow us to estimate the intermittency that can be resolved with the different UAS configurations. Measurements taken solely with the 1000 Hz reference sensors allow examination of the kurtosis curve across various τ values, even below the minimum time lags resolvable by the drones. At these small time lags, a high degree of intermittency can be observed, which could only be captured at time lags that are beyond the limits determined for the given variance of the respective drones (see Fig. 9). This behavior is consistent with expectations based on the wind tunnel setup and the applied active grid protocols.

https://doi.org/10.5194/egusphere-2026-4904
Preprint. Discussion started: 3 November 2026
© Author(s) 2026. CC BY 4.0 License.

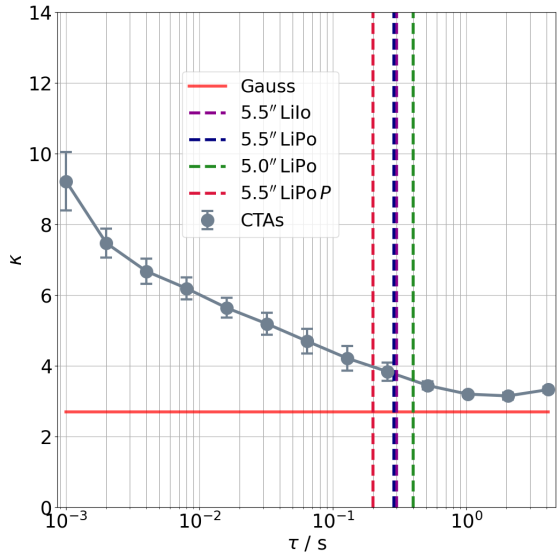
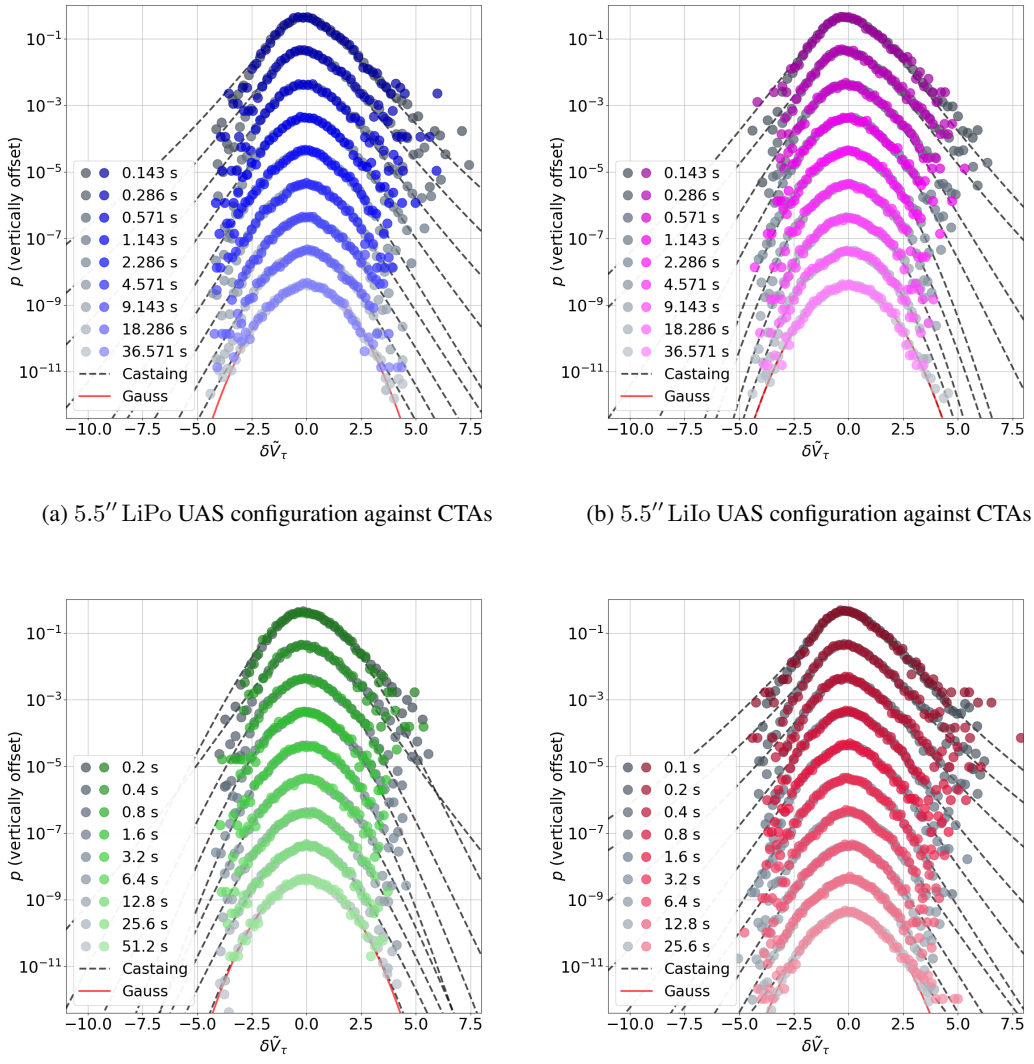


Figure 9. Behavior of the kurtosis κ of the probability density function of velocity increments for different time lags τ in a time series measured with the reference sensors in the wind tunnel. The grey curve shows the results from the reference CTAs, the horizontal red line represents the value of $\kappa = 3$ for a Gaussian probability density function, and the vertical dashed lines indicate the minimum achievable time lags for the various UAS configurations according to the identified sampling frequency f_s.

Comparisons of the PDFs of velocity increments within the measurement range achievable by the drones show good agreement between the drones and the reference sensors (see Fig. 10).

https://doi.org/10.5194/egusphere-2026-4904
Preprint. Discussion started: 3 November 2026
© Author(s) 2026. CC BY 4.0 License.



(a) $5.5''$ LiPo UAS configuration against CTAs

(b) $5.5''$ LiIo UAS configuration against CTAs

(c) $5.0''$ LiPo UAS configuration against CTAs

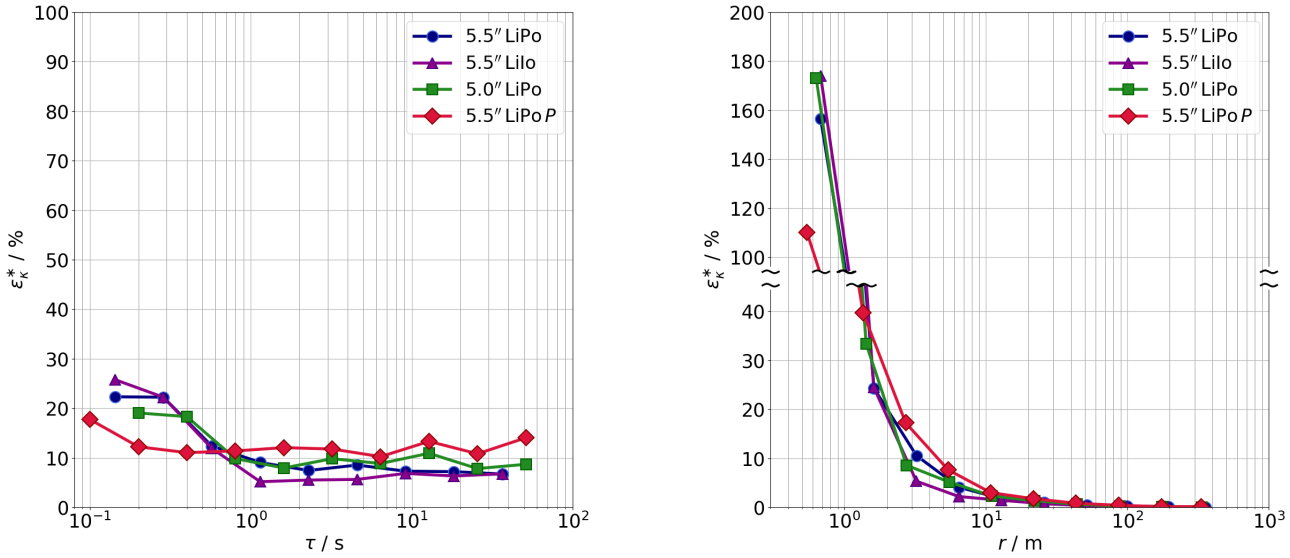
(d) $5.5''$ LiPo P UAS configuration against CTAs

Figure 10. Example comparisons of the probability density functions (PDFs) p of the velocity increments $\delta\tilde{V}_\tau$ for various time lags τ, measured using different UAS configurations in flow with identical wind tunnel settings. The grey markers show the respective data points from the reference CTA measurements, while the colored markers show the data points from the measurements with the respective UAS configuration. The red solid curve shows a Gaussian distribution as a reference, and the dashed black curves show the Castaing fit for each PDF. The PDFs are vertically offset from each other for improved visual clarity.

In principle, however, we can observe that, at very low wind speeds and the shortest τ values, all drone configurations show higher errors in capturing deviations from Gaussianity. This limits the turbulence resolution at the smallest scales, with errors

https://doi.org/10.5194/egusphere-2026-4904
Preprint. Discussion started: 3 November 2026
© Author(s) 2026. CC BY 4.0 License.

reaching approximately 20–27 % before decreasing to approximately 10 %, while they remain around 15 % for the padded configuration (Fig. 11a). Using the Taylor transformation, the temporal lags can be translated into spatial lags (see Fig. 11b), which shows a steady increase in measurement errors for shorter separations. In particular, increments at separations below 2 m can no longer be accurately detected by the drones.



(a) (b)

Figure 11. Comparison of the normalized root mean square error ε^* of the kurtosis κ for the probability density functions of velocity increments at different time lags τ (a) and after transformation into spatial lags r (b), based on time series measured by the different UAS configurations in the wind tunnel. The blue markers represent the data for our standard QAV250 configuration, while the other markers represent data from modified configurations based on it, with changes to the battery (purple), the propellers (green), and the autopilot mounting (red). The y-axis and curves in (b) are broken to resolve the lower-error range while retaining higher-error values. Note the different scales of the vertical axes between the two panels in the upper values.

4.3 Validation of turbulence retrieval

The validation results for the variance determination from field measurements of the various configurations are shown in Fig. 12.

https://doi.org/10.5194/egusphere-2026-4904
Preprint. Discussion started: 3 November 2026
© Author(s) 2026. CC BY 4.0 License.

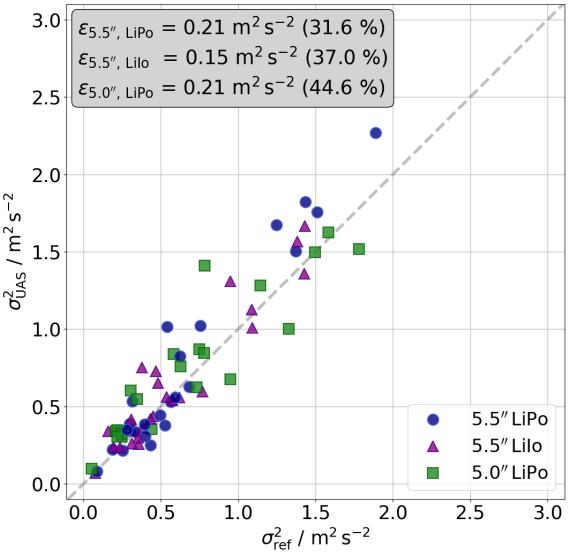
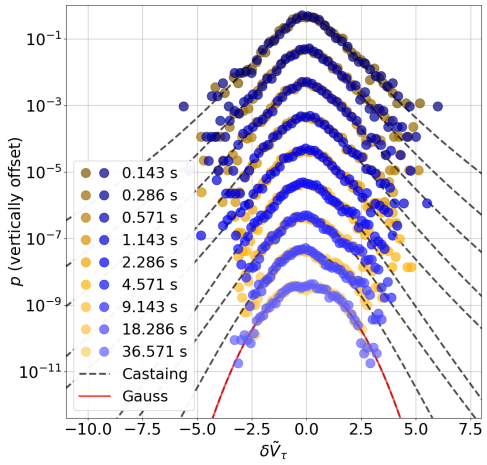


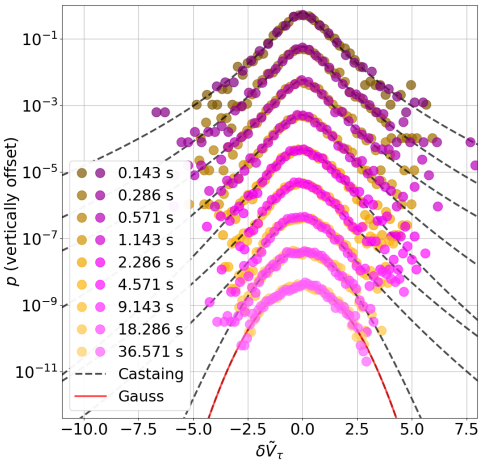
Figure 12. Comparison of the variances σ^2 of wind speeds determined from wind park measurements with different UAS configurations with those determined from the sonics. The blue markers represent the data for our standard QAV250 configuration, while the other markers represent data from modified configurations based on it, with changes to the battery (purple) and the propellers (green).

410 However, the overestimation of low variances no longer occurs for the $5.0''$ LiPo configuration and the accuracies among the configurations are comparable here as well. Validation of the measurement of velocity increments using the same dataset also shows good agreement between the UAS and reference measurement (see Fig. 13):

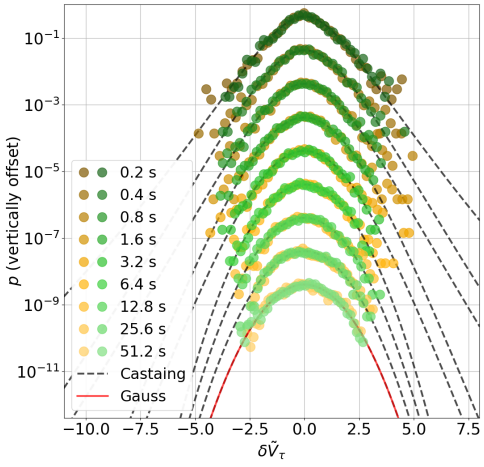
https://doi.org/10.5194/egusphere-2026-4904
Preprint. Discussion started: 3 November 2026
© Author(s) 2026. CC BY 4.0 License.



(a) $5.5''$ LiPo UAS configuration against sonic



(b) $5.5''$ LiIo UAS configuration against sonic



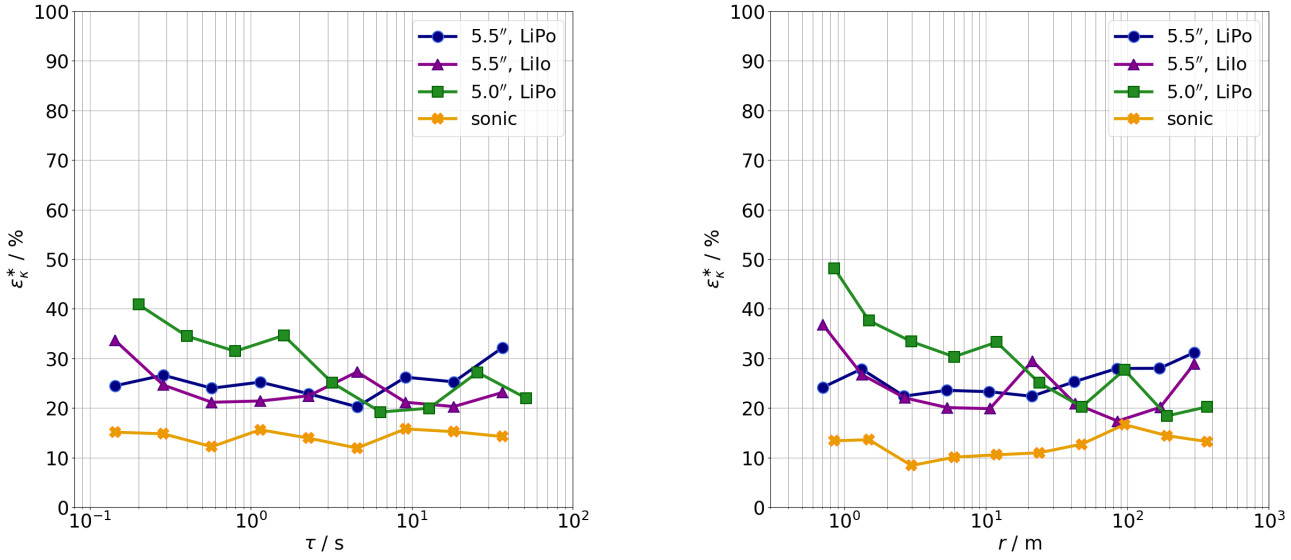
(c) $5.0''$ LiPo UAS configuration against sonic

Figure 13. Example comparisons of the probability density functions (PDFs) p of the normalized velocity increments $\delta\tilde{V}_\tau$ for various time lags τ, measured using different UAS configurations simultaneously in the same flow. The yellow markers show the respective data points from the reference sonic measurements, while the colored markers show the data points from the measurements obtained with the respective UAS configuration. The red solid curve shows a Gaussian distribution as a reference, and the dashed black curves show the Castaing fit for each PDF. The PDFs are vertically offset from each other for improved visual clarity.

When comparing the kurtosis of the velocity increments for all flights in the fleet, the relative error across all analyzed τ values is approximately 25 % for the $5.5''$ configurations. For the $5.0''$ configuration, the relative error is higher for $\tau < 3$ s,

https://doi.org/10.5194/egusphere-2026-4904
Preprint. Discussion started: 3 November 2026
© Author(s) 2026. CC BY 4.0 License.

with the nRMSE exceeding 40 % (Fig. 14a). This behavior remains largely consistent when converting the temporal lags into spatial lags (see Fig. 14b). The intrinsic error of κ derived from the reference sonics is between approximately 11 % and 17 % for all τ.



(a) (b)

Figure 14. Comparison of the normalized root mean square error ε^* of the kurtosis κ for the probability density functions of velocity increments at different time lags τ (a) and after transformation into spatial lags r (b), based on time series measured by the different UAS configurations in the wind park. The blue markers represent the data for our standard QAV250 configuration, while the other markers represent data from modified configurations based on it, with changes to the battery (purple), and the propellers (green). The yellow markers represent the intrinsic error derived from the sonic measurements.

The PDFs of sensor pairs from UASs and sonics with two lateral separations are shown in Fig. 15:

https://doi.org/10.5194/egusphere-2026-4904
Preprint. Discussion started: 3 November 2026
© Author(s) 2026. CC BY 4.0 License.

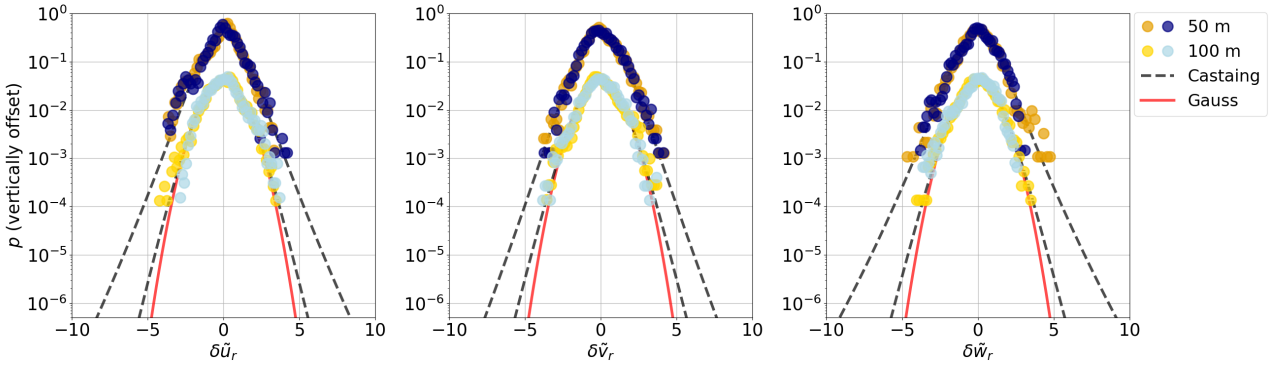


Figure 15. Example comparison of the probability density functions p of the normalized velocity increments of the 3D wind components $\delta\tilde{u}_r$, $\delta\tilde{v}_r$, and $\delta\tilde{w}_r$ at separation distances r, measured using the same UAS configuration against sonic anemometers at lateral separations of 50 m and 100 m. The blue markers show the respective data points from the UAS measurements, while the yellow markers show the data points from the measurements obtained with the respective sonic anemometers. The darker marker tones correspond to 50 m separation, and the brighter tones to 100 m separation. The solid red curve shows a Gaussian distribution as a reference, and the dashed black curves represent the Castaing fits. The PDFs are vertically offset from each other for improved visual clarity.

The PDFs show a deviation from a Gaussian distribution with more pronounced tips. Overall, there is a high degree of qualitative agreement between UASs and sonics, with the kurtosis values showing better agreement for the shorter distances. The differences are greatest for the vertical wind component. Fig. 16 shows the PDFs of vertically distributed sensor pairs from UASs and sonics.

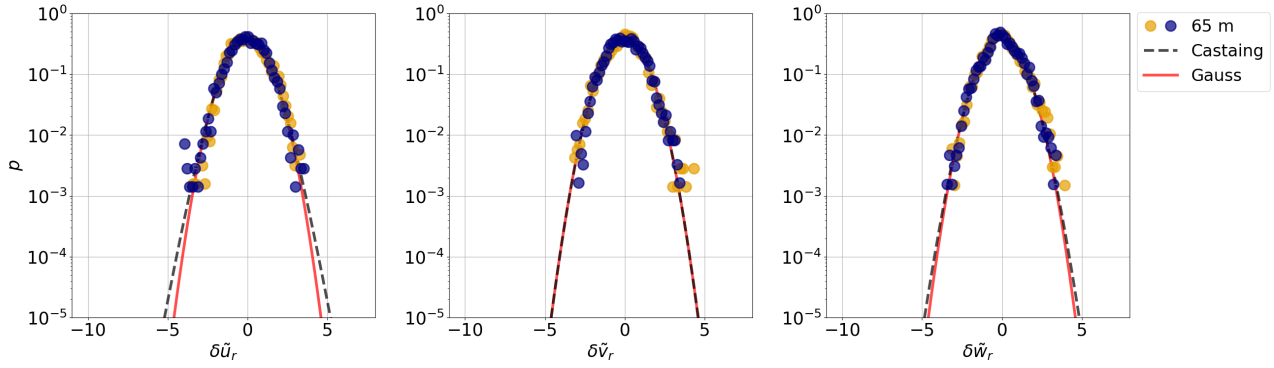


Figure 16. Example comparison of the probability density functions p of the normalized velocity increments of the 3D wind components $\delta\tilde{u}_r$, $\delta\tilde{v}_r$, and $\delta\tilde{w}_r$ at separation distance r, measured using the same UAS configuration against sonic anemometers at a vertical separation of 65 m. The blue markers show the respective data points from the UAS measurements, while the yellow markers show the data points from the measurements obtained with the respective sonic anemometers. The solid red curve shows a Gaussian distribution as a reference, and the dashed black curves represent the Castaing fits.

https://doi.org/10.5194/egusphere-2026-4904
Preprint. Discussion started: 3 November 2026
© Author(s) 2026. CC BY 4.0 License.

The general shapes of the PDFs from the UAS measurements reproduce the PDFs from the reference measurements and are generally close to a normal distribution, but display slightly elevated tails at times. The nRMSEs between the kurtosis values of the PDFs determined from UASs and sonics for all spatial separations and wind components are listed in Table 2:

Table 2. nRMSEs of the kurtosis of the probability density functions of increments for the 3D wind components and different spatial separations.

	κ_u	κ_v	κ_w
$\varepsilon^*_{\mathrm{lat,50\ m}}$	13.5 %	18.4 %	17.5 %
$\varepsilon^*_{\mathrm{lat,100\ m}}$	12.0 %	17.2 %	16.1 %
$\varepsilon^*_{\mathrm{ver,65\ m}}$	15.0 %	13.1 %	17.6 %

Fig. 17 shows the median magnitude-squared coherence of all measurements with laterally distributed sensor pairs at two different separation distances from UASs and sonics, respectively.

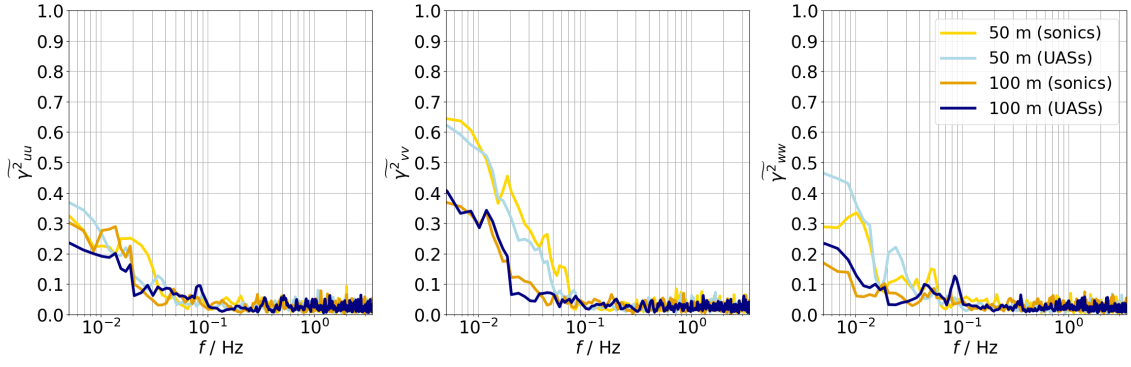


Figure 17. Comparison of the median magnitude-squared coherence $\widetilde{\gamma^2}$ for the frequencies f of the 3D wind components u, v and w, derived from all fleet measurements using the same UAS configurations against sonic anemometers at 50 m and 100 m lateral separation. The blue curves show the respective data points from the UAS measurements, while the yellow curves show the data points from the measurements with the respective sonic. The darker tones of marker colors are for 50 m, the brighter tones for 100 m separation.

In both measurement systems, the highest coherence values occur predominantly at low frequencies, with coherence decreasing significantly at higher frequencies. Coherence is generally higher at the shorter distance (50 m) than at the longer distance (100 m), which is particularly evident in the lateral and vertical wind components. The strongest agreement between UASs and sonics is observed for v in terms of both magnitude and the qualitative frequency-dependent trend. For u, the difference between the lateral distances is the smallest. The largest differences between the measurement systems occur at the lowest frequencies of the w component, with the UAS measurements showing higher coherence. In addition, the curves, especially

https://doi.org/10.5194/egusphere-2026-4904
Preprint. Discussion started: 3 November 2026
© Author(s) 2026. CC BY 4.0 License.

the UAS curves, exhibit narrow-band peaks at higher frequencies. The coherence of measurements from vertically separated UASs and sonics is shown in Fig. 18:

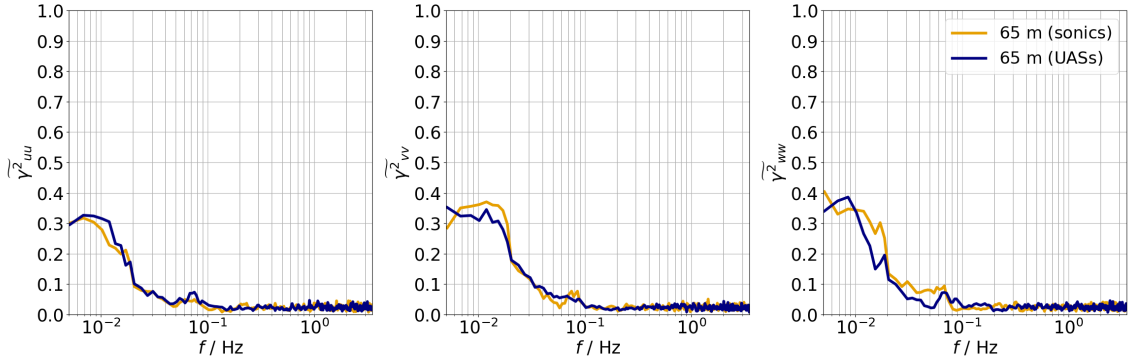


Figure 18. Comparison of the median magnitude-squared coherence $\widetilde{\gamma^2}$ as a function of frequency f for the 3D wind components u, v, and w, derived from all fleet measurements using the same UAS configuration against sonic anemometers at a vertical separation of 65 m. The blue curves show the respective data from the UAS measurements, while the yellow curves show the data from the measurements obtained with the respective sonic anemometers.

Also here, the highest coherence values in both measurement systems occur predominantly at low frequencies, with coherence decreasing significantly at higher frequencies. The agreement between UASs and sonics is generally very high, especially for the u component.

5 Discussion

When comparing the results of limit identification across the drones to address research question 1, it is noteworthy that the $5.0''$ propeller configuration exhibits the lowest frequency resolution. This contradicts our hypothesis prior to the experiments, which was that larger propellers would tend to dampen smaller turbulent vortices, thereby reducing high-frequency resolution. However, another effect is more significant here: For otherwise identical drone hardware under the same atmospheric conditions, the propeller thrust scales approximately with the square of the rotational speed and with the fourth power of the propeller diameter. Therefore, a propeller with a $10\,\%$ smaller diameter produces about $34\,\%$ less thrust at the same rotational speed. To generate the same thrust required for hovering, the smaller propeller must compensate for the reduced diameter by spinning about $24\,\%$ faster. These increased motor speeds lead to greater vibrations in the airframe, which affect the signal-to-noise ratio (SNR) in the accelerometers and which we consider to be the cause of the resolution limits. We had expected the significantly better resolution with the UAS configuration using pads, as this improves the SNR in the accelerometer and thus our measurement capability. As previously mentioned, however, the absolute accuracy of the wind estimate is susceptible to the individual calibration offset of each drone, which is less stable with damping pads. The improved temporal resolution must therefore be traded off against robust absolute accuracy.

https://doi.org/10.5194/egusphere-2026-4904
Preprint. Discussion started: 3 November 2026
© Author(s) 2026. CC BY 4.0 License.

The effect of overestimating high frequencies observed in the variance analysis in the wind tunnel using the $5.0''$ LiPo configuration has already been noted by Kistner et al. (2024). Using the same configuration, maximum resolvable frequencies of 2 Hz were also found by Wetz and Wildmann (2022). The identification of resolution limits in this work provides a better context for these results. The deviations in PSDs at higher frequencies, obtained from UAS measurements against reference measurements, are also found by Shelekhov et al. (2022), even though they are not as distinct as in our case. A distinct peak in the high-frequency range of the PSD from UAS measurements is also observed by Schurig et al. (2026), who also attribute this to vibrations induced by the rotors and transmitted to their sensor when using the direct wind measurement method.

In general, regarding the methodology, it should be noted that this study did not investigate any software-related influences on turbulence resolution. While minor tests involving changes to the controller settings did not appear to have any significant effect on vibrations, differences in the output acceleration signal between PX4 and ArduPilot were observed on the same drone hardware. Preliminary tests have shown that high-frequency noise appears to be filtered out more effectively in ArduPilot. However, no tests were conducted against reference measurements to verify this. A study of software-related influences could therefore be the subject of a separate investigation.

Regarding research question 2, during verification of the measurement accuracy for variance in the wind tunnel tests, only low errors are generally observed. The reproducibility of the drone measurements is very good. With the $5.5''$ LiPo configuration, deviations from the reference measurements are highest at high variances, whereas with the $5.0''$ LiPo configuration, the highest deviations occur in the low-variance range. This is caused by high-frequency noise at low variances, which is consistent with the lowest limits for f_{max}. This demonstrates how important it is to identify and apply a maximum sampling frequency for the measurements. However, it also shows that the applied frequency must still be verified and adjusted when using data from field measurements. A lower f_{s} would have already led to better accuracies in the wind tunnel tests for the $5.0''$ LiPo configuration. The reason for this is also a poorer SNR under these conditions, as well as the fact that the highest possible and thus optimistic maximum frequency was selected for downsampling during verification.

When applying the frequencies in data processing for increment analysis, we know that when sampling at 7 Hz, lags of at least three sampling steps, i.e. approximately 0.43 s, should be used for analyses of velocity increments to obtain more reliable results. This follows from the comparison of the kurtosis of the velocity increments, which shows that the deviation between UASs and the reference is primarily determined by the smallest spatial scales. While the relative error remains nearly constant across temporal lags, the deviation steadily increases with smaller lags after conversion using the Taylor hypothesis and is concentrated to a very large extent at the smallest spatial lag. For lags above 2 m, the error is very small. Therefore, the resolvable range for analyzing velocity increments, as determined by Taylor transformation, is limited to 2 m at small scales due to sensor limitations and is limited at larger scales by the maximum flight time. The largest scales analyzed in this work were over 350 m. Based on the wind turbines at the WiValdi research park, where the field validations were conducted, the range of 2 m to 350 m corresponds to approximately 0.02 to 3 times the rotor diameter of the wind turbines. This therefore covers a range corresponding to the turbulent scales expected to cause the most significant loads and fatigue on the structure.

Nevertheless, the experimental setup in the wind tunnel involves some methodological uncertainties that contribute to the quantified measurement uncertainties. In principle, the positioning using the optical flow sensor cannot be considered optimal,

https://doi.org/10.5194/egusphere-2026-4904
Preprint. Discussion started: 3 November 2026
© Author(s) 2026. CC BY 4.0 License.

which is why the drones sometimes move in the wind tunnel. This can affect wind measurements based on avionics data and increase uncertainties. Although the measurement setup described in Sec. 3, with the CTAs mounted at different heights, substantially reduced the disturbance of the reference sensors on the rear pole caused by the drone downwash, it could not eliminate this effect entirely. This increases the uncertainty of the reference measurements, as can be seen from the error bars for the reference values in Fig. 8. As a result, the deviations of the drones from the reference are usually within the uncertainty of the reference measurements. In the most extreme case, the standard deviations of the CTAs are 80 % higher during flights with a drone than during measurements without a drone. However, there are also significant deviations between the CTAs even without a drone (see Appendix C), which suggests a non-negligible inhomogeneity within the measurement volume. Since at most one CTA is disturbed at a time and only for a short period, while the other CTAs continue to measure undisturbed, and since the contribution of these disturbances to the uncertainty is smaller than the uncertainty caused by the measurement position in the flow, the measurements from all CTAs are included in the analyses.

The uncertainties identified during the validation flights confirm the results of the verification measurements, demonstrate the applicability of the method to field measurements, and thereby answer research question 3. The analysis further shows that the wind-speed variance and intermittency remain accurate even when all datasets are reprocessed using the most optimistic sampling frequency identified among the investigated flow conditions. Although lower sampling frequencies would be required to remain within the identified resolution limits for some individual cases, retaining the additional high-frequency components does not introduce a relevant bias in the derived variances. This can be attributed to the comparatively low PSD at these frequencies, such that their contribution to the integrated variance remains small. This result is particularly relevant for large datasets, such as those obtained during fleet campaigns. The variance initially derived using the optimistic sampling frequency for post-processing can be used in future to assess whether the respective dataset should subsequently be reprocessed at a lower sampling frequency only using drone data.

In the increment analyses conducted in the field measurements, the good agreement across most of the respective PDFs confirms the limits identified in the wind tunnel, and the measurements remain reliable even with just a single sample. In principle, within the respective limits of the drones, comparable measurement quality can also be observed across the $5.5''$ configurations with different batteries, while the $5.0''$ configuration exhibits larger uncertainties for smaller lags. However, it should be noted that larger deviations in kurtosis occur in comparison to the wind tunnel experiments when analyzing temporal lags.

When converting using the Taylor hypothesis, the uncertainty profile across the lags does not change as significantly as it does in the wind tunnel experiments. The difference between laboratory and field measurements suggests that the large error observed in the laboratory at the smallest spatial lag reveals a local resolution limit of the sensor. However, this signature does not appear in the field measurements. Nevertheless, the field measurements do not refute the small-scale sensor limitation observed in the wind tunnel. In fact, the absolute error between the drone and the reference is similarly large at comparable kurtosis values. In field measurements, however, comparable kurtosis values are already achieved at significantly larger lags. In other words, the turbulence of the wind at the wind park was more intermittent than the flow in the wind tunnel. At larger lags, the turbulent increments are larger, resulting in a more favorable SNR. The fact that a pronounced increase in error occurs

https://doi.org/10.5194/egusphere-2026-4904
Preprint. Discussion started: 3 November 2026
© Author(s) 2026. CC BY 4.0 License.

at the smallest spatial lag in the wind tunnel but not in the free field is therefore consistent with a lag-dependent sensitivity to sensor noise and finite sensor resolution.

The higher error at larger lags is most likely driven by uncertainties in the experimental setup in the wind park. In the validation measurements, the distance between the drones and the reference sonics is relatively large, which is particularly important to note when considering the uncertainties in the detection of smaller scales. The error between the drones and the reference should also be considered in the context of the intrinsic error in the reference measurements, which is already in the magnitude of 10–20 % and results from the finite duration of the measurements.

Addressing research question 4, we assess whether accurate turbulence analysis using combined measurements is possible under the identified constraints. The relative errors between UAS and sonic pairs in simultaneous and spatially distributed measurements of the kurtosis of the velocity increment PDFs are less than 20 % for all analyzed separation directions and all wind components. These errors are thus smaller than those associated with the analysis of spatial lags, which are determined using the Taylor hypothesis from temporal increments of measurements carried out with single drones (Fig. 14b). This confirms the need for simultaneous, spatially distributed measurements for this method of turbulence analysis. In addition, these errors are close to the intrinsic errors of the reference measurements determined in the single-point analysis, which are driven by the limited measurement period. The results therefore demonstrate that increment PDFs are characterized reliably using drones, particularly because simultaneous fleet measurements enable true spatial separations between measurement locations.

When determining coherence, the agreement between UASs and reference sensors is qualitatively good, as both systems exhibit high coherence at low frequencies and a clear decline in coherence at higher frequencies. Furthermore, UASs and sonics both show lower coherence over large distances than over smaller ones, which is consistent with the expectation that large-scale turbulent structures remain partially correlated over larger lateral distances, while smaller scales rapidly decorrelate. Furthermore, it can be clearly established that, for simultaneous, spatially distributed measurements with separation distances on the order of magnitude selected for this study, the maximum resolvable frequencies of all UAS configurations identified in the wind tunnel are sufficient to capture the coherence of the turbulence in all wind speed directions up to the frequencies at which coherence is observable.

In the coherence analyses of Wetz and Wildmann (2023), a significant decrease in coherence is observed at approximately 10^{-2} Hz for the lateral coherence of the horizontal wind when the drones are 70 m apart, which falls within the 50–100 m separation range of our experiment. Here, we can observe that coherence for u also decreases significantly, w still exhibits coherence for the 50 m distance but not for the 100 m distance, and v still shows coherence, both with the UASs and with the sonics. This demonstrates how the drones' 3D measurement capability enables more detailed coherence analyses through flexible in situ measurements.

The results of Thedin et al. (2023) are, in principle, comparable to those regarding coherence for lateral separation, particularly when considering that the results always depend on atmospheric conditions. For v, the highest coherence values at the lowest frequencies are 0.6 and 0.4 for the shorter and longer separation distances, respectively, and they decline at a comparable rate. However, in our results, no significant coherence is detectable beyond 0.05 Hz for the longer separation and beyond 0.08 Hz for the shorter separation, whereas Thedin et al. report a coherence of approximately 0.15 for the shorter separation. In

https://doi.org/10.5194/egusphere-2026-4904
Preprint. Discussion started: 3 November 2026
© Author(s) 2026. CC BY 4.0 License.

contrast, our measurements show higher coherence for the w component, at 0.2 and 0.4, respectively, for the two separations at the lowest frequencies, while Thedin et al. observed no coherence. For the u component, Thedin et al. report higher coherence at low frequencies for the shorter separation distance than we can detect. Even there, however, their results show a rapid decline and, in principle, lower coherence than for the lateral wind component. In general, the coherence for vertical separation reported by Thedin et al. is lower than that observed in our measurements. Our results show similar coherence behavior for u, v, and w. This differs from Thedin et al., for whom u is initially the most coherent component but also drops off rapidly, whereas v and w retain higher coherence at higher frequencies.

Thedin et al. (2023) generally note that coherence is highest for the velocity component aligned with the sensor separation. We observe this effect for all three separation directions and across all distances. This can be explained by the behavior of the two-point correlation function, which describes the longitudinal correlation for the velocity component parallel to the separation direction, whereas the other two components represent transverse correlations. Since the longitudinal two-point correlation is greater than the transverse correlation as the correlation function decreases, a larger common signal component between the two measurement points is retained for this component (Pope, 2000). This larger common component in the cross-spectrum manifests as correspondingly higher coherence.

In these comparisons with other studies, however, direct quantitative comparison is possible only to a limited extent, as the coherence curves presented here are derived from a combination of multiple individual measurements. As a result, measurement-related variations may be partially smoothed out or masked. Furthermore, the different measurement setups, sites, and situations must be taken into account.

Generally it should be emphasized that the focus of our analyses is on verifying the agreement between UAS and sonic measurements. Here, it can be observed that the coherence estimates obtained from the UASs and the reference measurements show close agreement. This agreement indicates that UAS measurements can be used in future meteorological studies to analyze the spatial coherence of all three wind components for separations along all three spatial directions, thereby providing further insight into atmospheric turbulence.

6 Conclusions

In this study, we first determined the resolvable spectral frequency range for turbulence measurements with various hardware configurations of a drone in order to enhance the processing of the logged avionics data for wind measurement. Here, the maximum resolvable frequencies for the different configurations are in the range of approximately 2.5 Hz to 5 Hz. Using wind measurements taken in the ForWind wind tunnel and at the DLR WiValdi research wind farm, the uncertainties in turbulence measurements for the various hardware configurations were verified and validated using single-point and two-point statistics. In this context, comparable accuracy in variance estimation was observed across the configurations, with an RMSE of $\leq 0.21\ \mathrm{m^2\,s^{-2}}$ compared to the reference sensors, and a high degree of agreement in the PDFs of the velocity increments between the UASs and the sonics, albeit with different minimum lags (2 m) due to the identified maximum resolvable frequencies. Furthermore, using multisensor analyses from simultaneous and spatially distributed fleet measurements with 10 UASs

https://doi.org/10.5194/egusphere-2026-4904
Preprint. Discussion started: 3 November 2026
© Author(s) 2026. CC BY 4.0 License.

in a single hardware configuration, we were able to extend the measurement capabilities of two-point statistical analyses to include spatial velocity increments and coherence analyses in all three spatial directions relative to the wind in order to evaluate the three-dimensional turbulence structure. With the demonstrated resolution of spatial turbulence at separation distances of 50 to 100 m, the potential of the box-shaped flight pattern was demonstrated, and a benchmark for ABL investigations using the SWUF-3D drone fleet was established based on the shown effects of hardware adjustments and quantified uncertainties. This will enable robust analyses of highly three-dimensional turbulent flows in complex terrain and behind wind turbines to be provided in the future. The box-shaped flight pattern used for these analyses can readily be adapted to different separation distances or extended to multiple interconnected boxes and can also complement measurements from meteorological masts or lidars, depending on the specific research question and experimental setup.

https://doi.org/10.5194/egusphere-2026-4904
Preprint. Discussion started: 3 November 2026
© Author(s) 2026. CC BY 4.0 License.

Appendix A: Calculation and bin-averaging of the power spectral density

The PSD quantifies the scale-dependent distribution of fluctuations and is calculated using the Fourier transform. It can be computed from acceleration data and, since we calculate wind speeds from the accelerations, also from a measured wind speed time series V sampled at frequency f_s. For such a time series, the discrete Fourier transform is defined as

$$\hat{V}_k = \sum_{j=0}^{N-1} V_j e^{-\mathrm{i}2\pi k j N^{-1}}, \qquad k = 0, \ldots, N-1. \tag{A1}$$

The frequency resolution is $\Delta f = f_\mathrm{s}/N$. The non-negative Fourier frequencies up to the Nyquist frequency are

$$f_k = \frac{k}{N} f_\mathrm{s}, \qquad k = 0, \ldots, N_h, \tag{A2}$$

with

$$N_h = \left\lfloor \frac{N}{2} \right\rfloor. \tag{A3}$$

For N, the one-sided PSD is given by

$$S_k = \begin{cases} \dfrac{1}{N f_\mathrm{s}} |\hat{V}_k|^2, & k = 0, \\ \dfrac{1}{N f_\mathrm{s}} |\hat{V}_k|^2, & k = \dfrac{N}{2} \text{ and } N \text{ is even}, \\ \dfrac{2}{N f_\mathrm{s}} |\hat{V}_k|^2, & 1 \le k \le N_h \text{ and } k \ne \dfrac{N}{2}, \end{cases} \qquad k = 0, \ldots, N_h. \tag{A4}$$

To reduce spectral scattering while maintaining the logarithmic scale dependence, the spectra are averaged over logarithmically distributed frequency bins. Let f_1 be defined as f_k for $k = 1$ and f_h for $k = N_h$. The bin boundary frequencies between f_1 and f_max are defined as

$$f_{b,j} = f_1 \left(\frac{f_h}{f_1} \right)^{j/B}, \qquad j = 0, \ldots, B. \tag{A5}$$

with B as the number of bins. The representative frequency of each logarithmic bin is chosen as the geometric mean:

$$\bar{f}_j = \sqrt{f_{b,j} f_{b,j+1}}, \qquad j = 0, \ldots, B-1. \tag{A6}$$

The indices of Fourier samples contained in the respective bin are

$$F_j = \{k : \; f_{b,j} \le f_k < f_{b,j+1}\}, \tag{A7}$$

where the upper limit is included in the last bin to obtain the highest resolved frequency. The resulting PSD is obtained from a frequency-weighted average:

$$\bar{S}(\bar{f}_j) = \frac{1}{|F_j|} \frac{1}{\bar{f}_j} \sum_{k \in F_j} S_k f_k, \qquad j = 0, \ldots, B-1. \tag{A8}$$

https://doi.org/10.5194/egusphere-2026-4904
Preprint. Discussion started: 3 November 2026
© Author(s) 2026. CC BY 4.0 License.

We use the Freedman–Diaconis rule (Freedman and Diaconis, 1981) on the logarithmic frequency axis to determine the number of bins based on the data using the interquartile range (IQR) I. With

$$s_k = \log_{10}(f_k), \qquad k = 1, \ldots, N_h, \tag{A9}$$

we obtain

$$I(s) = Q_{0.75}(s) - Q_{0.25}(s). \tag{A10}$$

With

$$h = 2\, I(s)\, N_h^{-1/3}, \tag{A11}$$

we calculate the number of bins as

$$B = \left\lceil \frac{\max(s) - \min(s)}{h} \right\rceil + 1. \tag{A12}$$

Appendix B: Comparison of the lowest resolvable power spectral densities

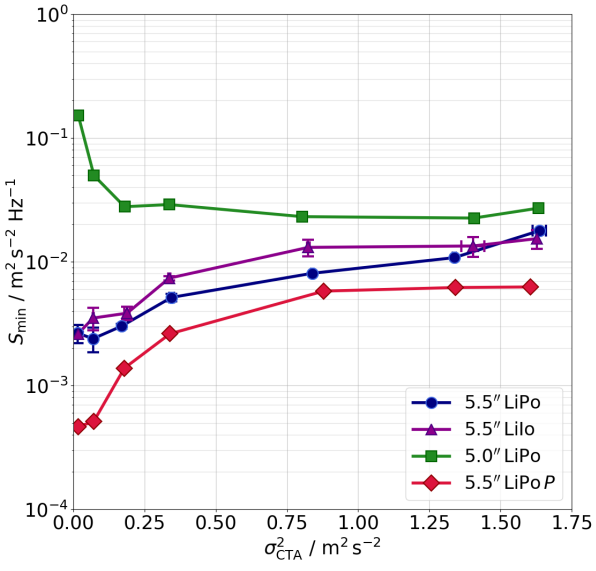
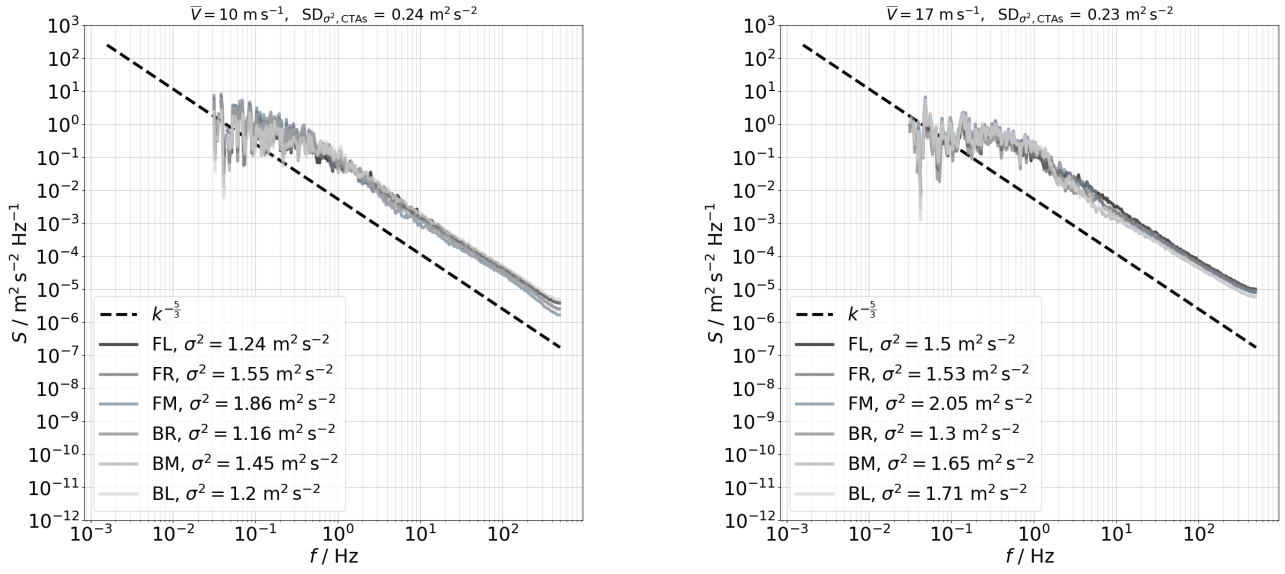


Figure B1. Comparison of the lowest power spectral density S_{min} that can be resolved with different UAS configurations at different levels of wind speed variance σ^2. The blue curve represents the data for our standard QAV250 configuration, while the other curves represent data from modified configurations based on it, with changes to the battery (purple), the propellers (green), and the autopilot mounting (red).

https://doi.org/10.5194/egusphere-2026-4904
Preprint. Discussion started: 3 November 2026
© Author(s) 2026. CC BY 4.0 License.

Appendix C: Characterization of local flow differences within the measurement volume



(a) (b)

Figure C1. Example comparisons of the bin-averaged power spectral density $\overline{S}$ and wind speed variance σ^2 determined with the six reference CTAs in the wind tunnel without a drone flying in the flow during the measurement. The positions are abbreviated according to the respective CTA location: front (F) or back (B) pole, and left (L), middle (M), or right (R) on the pole when facing against the wind. The dashed black line represents the spectrum corresponding to the Kolmogorov $-5/3$ power law. The respective standard deviations (SD) of the variances from the CTA measurements are 0.24 $\mathrm{m^2\,s^{-2}}$ for the experiment at 10 $\mathrm{m\,s^{-1}}$ mean wind speed (a) and 0.23 $\mathrm{m^2\,s^{-2}}$ for the experiment at 17 $\mathrm{m\,s^{-1}}$ (b).

https://doi.org/10.5194/egusphere-2026-4904
Preprint. Discussion started: 3 November 2026
© Author(s) 2026. CC BY 4.0 License.

Appendix D: Spatial measurements in longitudinal separation direction

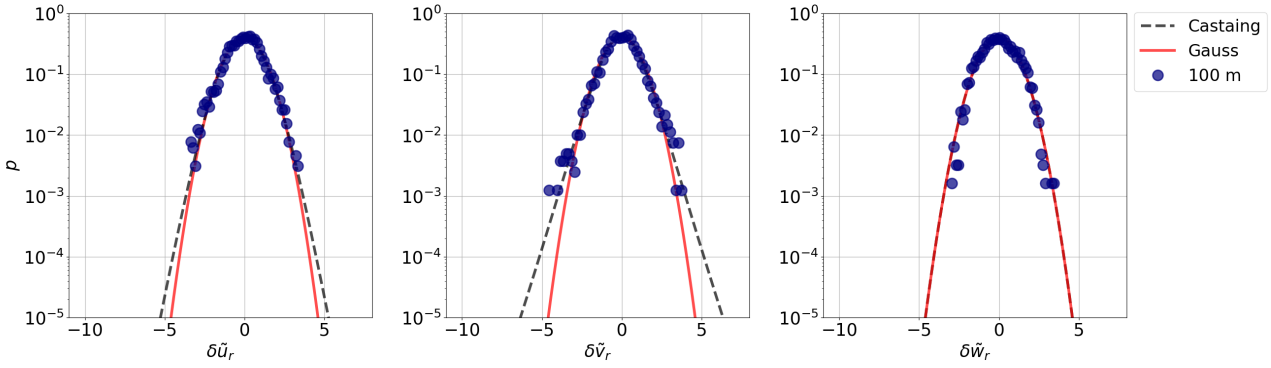


Figure D1. Exemplary measurement of the probability density functions p of the normalized velocity increments of the 3D wind components $\delta\tilde{u}_r$, $\delta\tilde{v}_r$, and $\delta\tilde{w}_r$ at separation distance r, measured using the same UAS configuration at a longitudinal separation of 100 m. The solid red curve shows a Gaussian distribution as a reference, and the dashed black curve represents the Castaing fit.

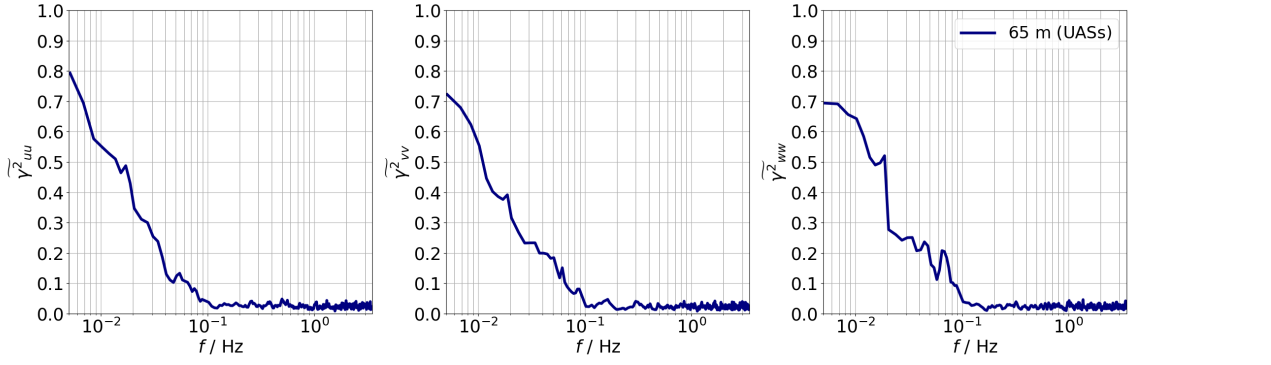


Figure D2. Median magnitude-squared coherence $\widetilde{\gamma^2}$ as a function of frequency f for the 3D wind components u, v, and w, derived from all fleet measurements using the same UAS configuration.

https://doi.org/10.5194/egusphere-2026-4904
Preprint. Discussion started: 3 November 2026
© Author(s) 2026. CC BY 4.0 License.

Appendix E: Tables

Table E1. Flight protocol for fleet flights in the configuration comparison pattern. UASs 11 and 12 are equipped with the 5.5″ LiIo configuration, UASs 13 and 14 with the 5.5″ LiPo configuration, and UASs 15 and 16 with the 5.0″ LiPo configuration.

Flight no.	UAS no.						Date	Time	Wind speed	TI	Wind dir.	Temp	Hum
	11	12	13	14	15	16		UTC	ms^{-1}	%	°	°C	%
30	×	×	×	×	×	×	16 Mar 2025	11:18	8.3	6	288	8.6	85
31	×	×	×	×	×	×	16 Mar 2025	11:40	8.5	9	285	8.4	85
32	×	×	×	×	×	×	16 Mar 2025	12:03	7.8	10	288	8.7	85
33	×	×	×	×	×	×	16 Mar 2025	13:31	7.2	13	278	9.3	100
35	×	×	×	×	×	×	16 Mar 2025	15:51	7.2	7	296	7.4	100
36	×	×	×	×	×	×	16 Mar 2025	16:15	6.9	8	301	7.0	100
37	×	×	×	×	×	×	16 Mar 2025	16:33	7.0	6	307	7.3	95
47	×	×	×		×	×	20 Mar 2025	12:37	4.5	27	254	3.6	38
48	×	×	×	×	×		20 Mar 2025	13:11	5.0	16	290	4.1	40
49	×	×	×	×	×		20 Mar 2025	13:55	4.2	9	304	4.7	44
50	×	×	×	×	×		20 Mar 2025	14:25	4.6	10	306	5.4	45
51	×	×	×		×		20 Mar 2025	14:50	4.0	14	308	14.1	45
52	×	×	×		×		20 Mar 2025	15:20	5.2	4	315	14.0	46

Table E2. Flight protocol for fleet flights in the box-shaped pattern. All UASs are equipped with the 5.5″ LiPo configuration.

Flight no.	UAS no.										Date	Time	Wind speed	TI	Wind dir.	Temp	Hum
	11	12	13	14	15	21	22	23	24	25		UTC	ms^{-1}	%	°	°C	%
36	×	×	×		×	×	×	×	×	×	22 Jul 2024	08:16	9.0	18	284	16.5	79
37	×	×	×	×	×	×	×	×	×	×	22 Jul 2024	08:54	9.2	15	286	16.7	75
38	×	×	×		×	×	×	×		×	22 Jul 2024	09:32	8.9	14	288	16.8	74
39	×	×		×	×	×		×	×	×	22 Jul 2024	10:30	8.7	16	288	17.1	71
40	×	×	×		×	×	×	×	×	×	22 Jul 2024	10:58	9.2	16	284	17.3	71
41	×	×	×	×	×	×	×	×	×	×	22 Jul 2024	11:33	9.4	15	278	17.0	71
42	×	×	×	×	×	×	×	×	×	×	22 Jul 2024	12:15	8.6	13	291	17.0	69
43	×	×	×	×	×	×	×	×	×	×	22 Jul 2024	12:53	8.2	13	297	16.9	70
44	×	×	×	×	×	×	×	×	×	×	22 Jul 2024	13:19	7.1	14	287	16.7	72

https://doi.org/10.5194/egusphere-2026-4904
Preprint. Discussion started: 3 November 2026
© Author(s) 2026. CC BY 4.0 License.

Table E3. Number of wind tunnel runs for each UAS configuration and the respective mean wind speed. The preset turbulence intensity is approximately 16.5 % for the runs with a speed preset of 10 m s^{-1} and approximately 11.5 % for the other runs.

Wind speed	UAS configuration			
$\mathrm{m\,s^{-1}}$	5.5″ LiPo	5.5″ LiIo	5.0″ LiPo	5.5″ LiPo P
3.0	2	2	1	1
5.0	2	2	1	1
7.0	2	2	1	1
9.0	2	2	1	1
10.0*	2	2	1	1
13.0	2	2	1	1
17.0	2	2	1	1

Table E4. Root mean square error of the wind speed measurement ε_V for each UAS configuration.

UAS configuration	ε_V
	$\mathrm{m\,s^{-1}}$
5.5″ LiPo	0.17
5.5″ LiIo	0.16
5.0″ LiPo	0.24
5.5″ LiPo P	0.17

https://doi.org/10.5194/egusphere-2026-4904
Preprint. Discussion started: 3 November 2026
© Author(s) 2026. CC BY 4.0 License.

Table E5. Nomenclature

ABL	atmospheric boundary layer
B	number of bins
$C_V(\tau)$	autocovariance
I	IQR
IQR	interquartile range
f	frequency
f_c	cutoff frequency
f_max	divergence frequency
f_s	sampling frequency
k	lag in sampling intervals
p	PDF
PDF	probability density function
PSD	power spectral density
r	separation distance
S	PSD
$S_{V_1V_2}(f)$	cross power spectral density of V_1 and V_2
$S_{V_1V_1}(f)$, $S_{V_2V_2}(f)$	auto power spectral densities of V_1 and V_2
SNR	signal-to-noise ratio
T	time interval
TI	turbulent intensity
u	longitudinal wind speed component in the flow-fixed coordinate system
v	lateral wind speed component in the flow-fixed coordinate system
V_i	measured wind speed time series
$\overline{V}$	mean wind speed
w	vertical wind speed component in the flow-fixed coordinate system
δV_τ	wind speed increment for time lag τ
$\delta\tilde{V}$	normalized wind speed increment
γ^2	magnitude-squared coherence
κ	kurtosis
Λ^2	shape factor
σ^2	wind speed variance
$\sigma_{\delta V_\tau}$	standard deviation of wind speed increments for time lag τ
τ	time lag between two values in the time series
$\overline{\delta V_\tau}$	mean wind speed increment for time lag τ
$\widetilde{\gamma^2}(f)$	median of coherence at frequency f

https://doi.org/10.5194/egusphere-2026-4904
Preprint. Discussion started: 3 November 2026
© Author(s) 2026. CC BY 4.0 License.



Data availability. The data is available under doi.org/10.5281/zenodo.20123351 .

Author contributions. JK wrote the main manuscript, conducted the experiments and performed the data analysis. TM was involved in the experimental setup of the wind tunnel measurements and wrote the description of the wind tunnel. JP contributed to the data analysis, interpretation of the results, and manuscript revision. NW contributed to the experimental setup, supervised the project, and contributed to the manuscript.

Competing interests. The authors declare that they have no conflict of interest.

Disclaimer. This research is part of the project ESTABLIS-UAS and has been supported by the HORIZON EUROPE European Research Council (grant no. 101040823). The article processing charges for this open access publication were covered by the German Aerospace Center (DLR).

Acknowledgements. Many thanks to Almut Alexa and Julian Jüchter for their intensive assistance and support during the wind tunnel experiments and to Lars Neuhaus for providing the protocols used to control the active grid. We thank Almut Alexa and Laszlo György for their efforts in supporting the field measurements. We also thank Michael Holling for his help in preparing the wind tunnel measurements. Manuel Moser reviewed the manuscript internally and we thank him for his valuable comments. We acknowledge the use of ChatGPT (OpenAI) to assist with Python code for figure preparation and with language editing. The authors performed the scientific analyses and interpretation and drew the conclusions, and remain fully responsible for the manuscript content. Pixhawk is a trademark of Lorenz Meier.

https://doi.org/10.5194/egusphere-2026-4904
Preprint. Discussion started: 3 November 2026
© Author(s) 2026. CC BY 4.0 License.

References

Bowen, A. J., Flay, R. G. J., and Panofsky, H. A.: Vertical coherence and phase delay between wind components in strong winds below 20 m, 26, 313–324, https://doi.org/10.1007/bf00119530, 1983.

Bramati, M., Savvakis, V., Beyrich, F., Bange, J., and Platis, A.: In Situ Uncrewed Aircraft Measurements of Turbulent Kinetic Energy over Heterogeneous Terrain, 42, 319–338, https://doi.org/10.1175/jtech-d-24-0026.1, 2025.

Brosy, C., Krampf, K., Zeeman, M., Wolf, B., Junkermann, W., Schäfer, K., Emeis, S., and Kunstmann, H.: Simultaneous multicopter-based air sampling and sensing of meteorological variables, Atmospheric Measurement Techniques, 10, 2773–2784, https://doi.org/10.5194/amt-10-2773-2017, 2017.

Böttcher, F., Barth, S., and Peinke, J.: Small and large scale fluctuations in atmospheric wind speeds, 21, 299–308, https://doi.org/10.1007/s00477-006-0065-2, 2006.

Canter, C. A. and Bailey, S. C. C.: Spatially Sampled Measurements of Atmospheric Turbulence Using Unmanned Aerial Vehicles, in: 11th International Symposium on Turbulence and Shear Flow Phenomena (TSFP11), Southampton, UK, july 30–August 2, 2019, 2019.

Castaing, B., Gagne, Y., and Hopfinger, E.: Velocity probability density functions of high Reynolds number turbulence, 46, 177–200, https://doi.org/10.1016/0167-2789(90)90035-n, 1990.

Chen, D., Su, W., Jiang, S., Yang, H., Zhang, C., Jiang, S., Chang, D., Liang, Y., Wang, H., Yang, X., Fu, T.-M., Zeng, Z., Zhu, L., Shen, H., Wang, C., and Ye, J.: Wind estimation based on flight dynamics of unmanned aerial vehicle: influencing variables and its environmental application, 26, 3607–3620, https://doi.org/10.5194/acp-26-3607-2026, 2026.

Chillà, F., Peinke, J., and Castaing, B.: Multiplicative Process in Turbulent Velocity Statistics: A Simplified Analysis, 6, 455–460, https://doi.org/10.1051/jp2:1996191, 1996.

Freedman, D. and Diaconis, P.: On the histogram as a density estimator:L 2 theory, 57, 453–476, https://doi.org/10.1007/bf01025868, 1981.

Ghirardelli, M., Kral, S. T., Cheynet, E., and Reuder, J.: SAMURAI-S: Sonic Anemometer on a Multi-Rotor drone for Atmospheric turbulence Investigation in a Sling load configuration, 18, 2103–2124, https://doi.org/10.5194/amt-18-2103-2025, 2025.

González-Rocha, J., Woolsey, C. A., Sultan, C., and Wekker, S. F. J. D.: Sensing Wind from Quadrotor Motion, Journal of Guidance, Control, and Dynamics, 42, 836–852, https://doi.org/10.2514/1.g003542, 2019.

Hofmann, P.: Weiterentwicklung der Beobachtungsfähigkeit von Methanemissionen über drohnengestützte Messungen mittes low-cost Sensoren, https://elib.dlr.de/212711/, 2025.

Kim, S.-H., Kim, J.-H., Kim, J., and Min, J.-S.: Analyses of Atmospheric Turbulence Near Surface Observed by Uncrewed Aerial Vehicle in the Suburban Area of Seoul Metropolitan, South Korea, Geophysical Research Letters, 53, e2025GL119 855, https://doi.org/10.1029/2025GL119855, 2026.

Kistner, J., Neuhaus, L., and Wildmann, N.: High-resolution wind speed measurements with quadcopter uncrewed aerial systems: calibration and verification in a wind tunnel with an active grid, 17, 4941–4955, https://doi.org/10.5194/amt-17-4941-2024, 2024.

Kistner, J., Jüchter, J., and Wildmann, N.: High-resolution vertical wind and turbulence measurements with quadcopter uncrewed aerial systems: wind tunnel calibration and field validation, https://doi.org/10.48550/ARXIV.2603.19989, 2026.

Kosović, B., Basu, S., Berg, J., Berg, L. K., Haupt, S. E., Larsén, X. G., Peinke, J., Stevens, R. J. A. M., Veers, P., and Watson, S.: Impact of atmospheric turbulence on performance and loads of wind turbines: knowledge gaps and research challenges, 11, 509–555, https://doi.org/10.5194/wes-11-509-2026, 2026.

https://doi.org/10.5194/egusphere-2026-4904
Preprint. Discussion started: 3 November 2026
© Author(s) 2026. CC BY 4.0 License.



Krug, D., Baars, W. J., Hutchins, N., and Marusic, I.: Vertical Coherence of Turbulence in the Atmospheric Surface Layer: Connecting the Hypotheses of Townsend and Davenport, 172, 199–214, https://doi.org/10.1007/s10546-019-00445-4, 2019.

Kröger, L., Frederik, J., van Wingerden, J.-W., Peinke, J., and Hölling, M.: Generation of user defined turbulent inflow conditions by an active grid for validation experiments, Journal of Physics: Conference Series, 1037, 052 002, https://doi.org/10.1088/1742-6596/1037/5/052002, 2018.

Laubrich, T., Ghasemi, F., Peinke, J., and Kantz, H.: Statistical analysis of wind speed fluctuation and increments of non-stationary atmospheric boundary layer turbulence, https://doi.org/10.48550/ARXIV.0811.3337, 2008.

Molter, C. and Cheng, P. W.: ANDroMeDA - A Novel Flying Wind Measurement System, Journal of Physics: Conference Series, 1618, 032 049, https://doi.org/10.1088/1742-6596/1618/3/032049, 2020.

Morales, A., Wächter, M., and Peinke, J.: Characterization of wind turbulence by higher-order statistics, 15, 391–406, https://doi.org/10.1002/we.478, 2011.

Neuhaus, L., Berger, F., Peinke, J., and Hölling, M.: Exploring the capabilities of active grids, Experiments in Fluids, 62, https://doi.org/10.1007/s00348-021-03224-5, 2021.

Neumann, P. P. and Bartholmai, M.: Real-time wind estimation on a micro unmanned aerial vehicle using its inertial measurement unit, Sensors and Actuators A: Physical, 235, 300–310, https://doi.org/10.1016/j.sna.2015.09.036, 2015.

Nyquist, H.: Certain Factors Affecting Telegraph Speed, 3, 324–346, https://doi.org/10.1002/j.1538-7305.1924.tb01361.x, 1924.

Palomaki, R. T., Rose, N. T., van den Bossche, M., Sherman, T. J., and Wekker, S. F. J. D.: Wind Estimation in the Lower Atmosphere Using Multirotor Aircraft, Journal of Atmospheric and Oceanic Technology, 34, 1183–1191, https://doi.org/10.1175/jtech-d-16-0177.1, 2017.

Pfister, L., Gohm, A., Kossmann, M., Wieser, A., Babić, N., Handwerker, J., Wildmann, N., Vogelmann, H., Baumann-Stanzer, K., Alexa, A., Lapo, K., Paunović, I., Leinweber, R., Sedlmeier, K., Lehner, M., Hieden, A., Speidel, J., Federer, M., and Rotach, M.: The TEAMx-PC22 Alpine field campaign – Objectives, instrumentation, and observed phenomena, 33, 199–228, https://doi.org/10.1127/metz/2024/1214, 2024.

Pope, S. B.: Turbulent Flows, Cambridge University Press, ISBN 9780511840531, https://doi.org/10.1017/cbo9780511840531, 2000.

Rautenberg, A., Allgeier, J., Jung, S., and Bange, J.: Calibration Procedure and Accuracy of Wind and Turbulence Measurements with Five-Hole Probes on Fixed-Wing Unmanned Aircraft in the Atmospheric Boundary Layer and Wind Turbine Wakes, Atmosphere, 10, 124, https://doi.org/10.3390/atmos10030124, 2019.

Schottler, J., Reinke, N., Hölling, A., Whale, J., Peinke, J., and Hölling, M.: On the impact of non-Gaussian wind statistics on wind turbines – an experimental approach, 2, 1–13, https://doi.org/10.5194/wes-2-1-2017, 2017.

Schottler, J., Bartl, J., Mühle, F., Sætran, L., Peinke, J., and Hölling, M.: Wind tunnel experiments on wind turbine wakes in yaw: redefining the wake width, 3, 257–273, https://doi.org/10.5194/wes-3-257-2018, 2018.

Schurig, F., Schmid, C., Libardi, N. C., and Held, A.: Validation of a UAV-Based Multi-Sensor Fusion Approach for High-Frequency Wind Measurements at the WINSENT Test Site, 3224, 022 029, https://doi.org/10.1088/1742-6596/3224/2/022029, 2026.

Segales, A. R., Bell, T. M., Tasim, A. A., Quiroz, A., Simms, J. D., Gebauer, J. G., and Smith, E. N.: CopterSonde-SWX: development of a UAS-based Vertical Atmospheric Profiler for severe weather, 19, 3667–3686, https://doi.org/10.5194/amt-19-3667-2026, 2026.

Shelekhov, A., Afanasiev, A., Shelekhova, E., Kobzev, A., Tel'minov, A., Molchunov, A., and Poplevina, O.: Low-Altitude Sensing of Urban Atmospheric Turbulence with UAV, Drones, 6, 61, https://doi.org/10.3390/drones6030061, 2022.

Sim, S.-K., Maass, P., and Roman, H. E.: Distributions and Correlation Properties of Offshore Wind Speeds and Wind Speed Increments, 190, https://doi.org/10.1007/s10546-024-00889-3, 2024.

https://doi.org/10.5194/egusphere-2026-4904
Preprint. Discussion started: 3 November 2026
© Author(s) 2026. CC BY 4.0 License.

Stiperski, I., Rotach, M. W., Ansorge, C., Baklanov, A., Belušić, D., Bou-Zeid, E., Brun, C., Christen, A., Dias, N. L., Dörnbrack, A., Foken, T., Grachev, A., Holtslag, A. A., Kelly, M., Klein, P., Kosović, B., Meneveau, C., Mortarini, L., Patton, E. G., Steeneveld, G.-J., Thomas, C., Trini Castelli, S., and Zardi, D.: Open questions in atmospheric turbulence: A synthesis from the centenary workshop "100 years of turbulence: Innsbruck 1922 -2022", 3, 100 022, https://doi.org/10.1016/j.jemets.2025.100022, 2025.

Taylor, G. I.: The Spectrum of Turbulence, Proceedings of the Royal Society of London. A. Mathematical and Physical Sciences, 164, 476–490, https://doi.org/10.1098/rspa.1938.0032, 1938.

Thedin, R., Quon, E., Churchfield, M., and Veers, P.: Investigations of correlation and coherence in turbulence from a large-eddy simulation, Wind Energy Science, 8, 487–502, https://doi.org/10.5194/wes-8-487-2023, 2023.

Thielicke, W., Hübert, W., Müller, U., Eggert, M., and Wilhelm, P.: Towards accurate and practical drone-based wind measurements with an ultrasonic anemometer, Atmospheric Measurement Techniques, 14, 1303–1318, https://doi.org/10.5194/amt-14-1303-2021, 2021.

Tong, C., Mayor, S. D., Oncley, S. P., Roden, C., Brown, W. O. J., Spuler, S. M., Hayman, M., Morley, B. M., Witte, J., Dérian, P., De Wekker, S. F. J., Sun, J., Barskov, K., and Pourabdollah, D.: Multipoint Monin–Obukhov Similarity Theory Horizontal Array Turbulence Study (M2HATS), 107, E501–E527, https://doi.org/10.1175/bams-d-24-0037.1, 2026.

Wetz, T. and Wildmann, N.: Spatially distributed and simultaneous wind measurements with a fleet of small quadrotor UAS, Journal of Physics: Conference Series, 2265, 022 086, https://doi.org/10.1088/1742-6596/2265/2/022086, 2022.

Wetz, T. and Wildmann, N.: Multi-point in situ measurements of turbulent flow in a wind turbine wake and inflow with a fleet of uncrewed aerial systems, Wind Energy Science, 8, 515–534, https://doi.org/10.5194/wes-8-515-2023, 2023.

Wetz, T., Wildmann, N., and Beyrich, F.: Distributed wind measurements with multiple quadrotor unmanned aerial vehicles in the atmospheric boundary layer, Atmospheric Measurement Techniques, 14, 3795–3814, https://doi.org/10.5194/amt-14-3795-2021, 2021.

Wetz, T., Zink, J., Bange, J., and Wildmann, N.: Analyses of Spatial Correlation and Coherence in ABL Flow with a Fleet of UAS, Boundary-Layer Meteorology, https://doi.org/10.1007/s10546-023-00791-4, 2023.

Wildmann, N. and Győry, L.: Towards sensible heat flux measurements with fast-response fine-wire platinum resistance thermometers on small multicopter uncrewed aerial systems, 18, 5527–5544, https://doi.org/10.5194/amt-18-5527-2025, 2025.

Wildmann, N. and Kistner, J.: An evaluation of different measurement strategies to measure wind turbine near wake flow with small multicopter UAS, 2767, 042 004, https://doi.org/10.1088/1742-6596/2767/4/042004, 2024.

Wildmann, N. and Kistner, J.: In situ measurements of near wake dynamics with a fleet of multicopter drones, 3016, 012 011, https://doi.org/10.1088/1742-6596/3016/1/012011, 2025.

Wildmann, N., Rau, G. A., and Bange, J.: Observations of the Early Morning Boundary-Layer Transition with Small Remotely-Piloted Aircraft, Boundary-Layer Meteorology, 157, 345–373, https://doi.org/10.1007/s10546-015-0059-z, 2015.

Wächter, M., Heißelmann, H., Hölling, M., Morales, A., Milan, P., Mücke, T., Peinke, J., Reinke, N., and Rinn, P.: Wind Energy and the Turbulent Nature of the Atmospheric Boundary Layer, https://doi.org/10.48550/ARXIV.1202.2245, 2012.

Yang, Y., Zhang, Y., Han, T., Xie, C., Liu, Y., Huang, Y., Zhou, J., Sun, H., Zhao, D., Zhang, K., and Li, S.-M.: A correction algorithm for rotor-induced airflow and flight attitude changes during three-dimensional wind speed measurements made from a rotary unoccupied aerial vehicle, 18, 3035–3050, https://doi.org/10.5194/amt-18-3035-2025, 2025.